Monthly Notices
of the
ROYAL ASTRONOMICAL SOCIETY

MNRAS **460,** 1758–1789 (2016)
Advance Access publication 2016 May 6

doi:10.1093/mnras/stw1054

Optical emission line nebulae in galaxy cluster cores 1: the morphological, kinematic and spectral properties of the sample

S. L. Hamer,[1⋆] A. C. Edge,[2] A. M. Swinbank,[2] R. J. Wilman,[3] F. Combes,[4] P. Salomé,[4] A. C. Fabian,[5] C. S. Crawford,[5] H. R. Russell,[5] J. Hlavacek-Larrondo,[6] B. R. McNamara[7] and M. N. Bremer[8]

[1]*CRAL, Observatoire de Lyon, CNRS, Université Lyon 1, 9 Avenue Charles André, F-69561 Saint Genis-Laval, France*
[2]*Department of Physics, Institute for Computational Cosmology, Durham University, South Road, Durham DH1 3LE, UK*
[3]*Department of Physics, Durham University, South Road, Durham DH1 3LE, UK*
[4]*LERMA Observatoire de Paris, CNRS, 61 rue de l'Observatoire, F-75014 Paris, France*
[5]*Institute of Astronomy, University of Cambridge, Madingley Road, Cambridge CB1 0HA, UK*
[6]*Département de Physique, Université de Montréal, C.P. 6128, Succ. Centre-Ville, Montréal, Québec H3C 3J7, Canada*
[7]*Department of Physics and Astronomy, University of Waterloo, Waterloo, ON N2L 3G1, Canada*
[8]*H H Wills Physics Laboratory, Tyndall Avenue, Bristol BS8 1TL, UK*

Accepted 2016 May 3. Received 2016 May 1; in original form 2014 August 29

ABSTRACT

We present an Integral Field Unit survey of 73 galaxy clusters and groups with the VIsible Multi Object Spectrograph on the Very Large Telescope. We exploit the data to determine the Hα gas dynamics on kpc scales to study the feedback processes occurring within the dense cluster cores. We determine the kinematic state of the ionized gas and show that the majority of systems ($\sim$2/3) have relatively ordered velocity fields on kpc scales that are similar to the kinematics of rotating discs and are decoupled from the stellar kinematics of the brightest cluster galaxy. The majority of the Hα flux (>50 per cent) is typically associated with these ordered kinematics and most systems show relatively simple morphologies suggesting they have not been disturbed by a recent merger or interaction. Approximately 20 per cent of the sample (13/73) have disturbed morphologies which can typically be attributed to active galactic nuclei activity disrupting the gas. Only one system shows any evidence of an interaction with another cluster member. A spectral analysis of the gas suggests that the ionization of the gas within cluster cores is dominated by non-stellar processes, possibly originating from the intracluster medium itself.

Key words: galaxies: clusters: general – galaxies: elliptical and lenticular, cD.

1 INTRODUCTION

One of the key issues for our understanding of galaxy formation and evolution is the mechanism through which feedback from a galaxy affects the cooling of gas surrounding it. Simulations of galaxy formation which ignore non-gravitational heating (e.g. Katz & White 1993) produce a galaxy population with an excess of massive galaxies when compared to the observed Universe. This occurs as a result of gas cooling being constrained only by its density, which results in rapid cooling and an overproduction of stars in the dense clumps where galaxies form. To address this problem, the injection of energy into the gas from non-gravitational processes within the galaxies is invoked, a process dubbed 'feedback'. By including feedback in the simulations, the overproduction of massive galaxies is stopped resulting in a galaxy population in closer agreement to that which is observed (Bower et al. 2006; Croton et al. 2006).

While feedback is widely accepted as the means to slow the cooling of gas, the form that it takes is a highly debated topic. At face value, X-ray observations of the central regions of massive galaxy clusters show intense X-ray emission suggesting that the intracluster medium (ICM) is undergoing significant radiative cooling (Fabian et al. 1981). This rapidly cooling gas should condense into cold gas clouds and/or form stars on short time-scales relative to the age of the cluster (Fabian 1994). However, the cold gas mass (Braine & Dupraz 1994; McNamara & Jaffe 1994; O'Dea et al. 1994; Edge 2001; Salomé & Combes 2003) and star formation rates observed (McNamara & O'Connell 1989) are too low to be consistent with the mass of gas that should be cooling from the ICM.

Early observations with *XMM–Newton's* highly sensitive Reflection Grating Spectrometer failed to detect the X-ray spectral features of gas cooling at $\sim$1 keV (Peterson et al. 2001; Tamura et al. 2001; Peterson et al. 2003). The apparent lack of gas at X-ray

⋆E-mail: stephen.hamer@univ-lyon1.fr

temperatures of <1 keV suggests that some process is truncating the cooling to lower temperatures and preventing much of the gas from cooling further (see the review by Peterson & Fabian 2006). However, as the ICM core is still radiating away most of its energy through X-ray emission at a high rate, there must be some process acting in the cores of cooling flow clusters which is continually re-heating the gas. Thus 'feedback' from non-gravitational processes needs to be invoked in order to inject energy into the ICM and balance the effects of X-ray cooling. Many possible contributors to ICM heating have been suggested such as starbursts (Veilleux, Cecil & Bland-Hawthorn 2005), shocks from mergers (Markevitch & Vikhlinin 2007), sloshing of gas (ZuHone, Markevitch & Johnson 2010), conduction from the surrounding ICM (Voigt & Fabian 2004) and mechanical or radiative feedback from an active galactic nuclei (AGN; McNamara et al. 2005; McNamara & Nulsen 2007).

For the most rapidly cooling cluster cores, the brightest cluster galaxies (BCGs) ubiquitously exhibit optical line emission (Heckman et al. 1989; Cavagnolo et al. 2008). Crawford et al. (1999) found significant line emission in 32 per cent of a sample of 201 BCGs selected from the brightest cluster survey (BCS) X-ray selected sample (Ebeling et al. 1998). This line-emitting gas at 10^4 K traces filamentary structures around the BCG (Hatch et al. 2005, 2006; McDonald, Veilleux & Mushotzky 2011) and direct comparison has shown qualitatively similar structures in the 10^7 K X-ray (Fabian et al. 2008) and 30 K molecular (Salomé et al. 2011) gas. This structural similarity suggests that the gas phases are linked with gas from the ICM cooling through the warm phase before quickly condensing out into cold molecular gas clouds. However, the masses of the gas at these temperatures are not consistent with that predicted from cooling (Johnstone, Fabian & Nulsen 1987). Once the gas is in molecular clouds, ionizing radiation from within the cluster core can easily re-ionize and excite the surface of the gas clouds allowing the ionized gas to act as a proxy for the molecular gas.

Early studies of the brightest handful of BCGs showed a variety of complex spatial and velocity structures present in the ionized gas (Crawford et al. 2002; Hatch et al. 2006; Wilman, Edge & Swinbank 2006; Edwards et al. 2009). These early studies are highly suggestive, with some objects showing rotation, offset emission and most having largely uniform [N II]/Hα ratios. They also show that the most kinetically disturbed objects tend to be those which show evidence of a recent interaction. The presence of strong radio sources from the BCG at the centre of clusters (Burns et al. 1994; Hogan et al. 2015) further complicates the situation. In several clusters, the intricate filamentary structures formed by the optical line emission appear to be spatially and dynamically linked to the expanding radio lobes (Conselice, Gallagher & Wyse 2001; Hatch et al. 2006), the most clear example of this is NGC 1275 in the core of the Perseus cluster.

In order to place constraints on the BCG population, in general, we have used the VIsible Multi Object Spectrograph (VIMOS) on the Very Large Telescope (VLT) to obtain spatially resolved spectroscopy around the redshifted Hα emission of 73 BCGs, spanning a range in radio power, selected to show evidence of extended line emission structures. By using this representative sample, we will attempt to address three key questions pertinent to our understanding of cluster cores.

(i) What fraction of line-emitting BGCs are highly disturbed?: previous integral field unit (IFU) observations of just a handful of objects indicated the presence of gas at high velocity with structures and kinematics suggesting possible interactions with other cluster members (Wilman et al. 2006).

(ii) What role does the brightest cluster galaxy play in the cooling of gas from the ICM?: most clusters of galaxies have brightest cluster galaxies whose positions are strongly correlated with the cluster core (Peres et al. 1998; Sanderson, Edge & Smith 2009; Hudson et al. 2010). In Hamer et al. (2012), we identified three objects (two from this sample) in which the presence of ionized and molecular gas at the location of the core suggested that cooling continued despite being offset from the BCG. The systems studied in Hamer et al. (2012) had very large physical offsets but are rare.

(iii) What role does the cold gas play in the feedback process and how is feedback fuelled?: the degree of fine tuning required for feedback to be well regulated suggests a link between the non-gravitational processes in the BCG and the gas cooling from the ICM. In Hamer et al. (2014), we showed that Hydra-A contains a cold gas disc which may be responsible for moving gas into the vicinity of the AGN where it can fuel the powerful jets which are injecting mechanical energy into the ICM. If such kinematic structures are common, then discs may be an important component in regulating the feedback process.

In Section 2, we present details of the observations, data reduction and analysis techniques used throughout this study. We then present the observational parameters (Section 2.4) and study the maps from individual channels of the IFU in Section 3. Section 4 then presents the analysis of the morphology and kinematics of the sample. In Section 5, we study the physical condition of the gas in the ionized nebula through its spectral properties. In Section 6, we present a discussion of our findings with regard to the questions posed earlier in this Introduction. Finally, we present a summary of our findings and the conclusions we draw from them in Section 7.

Throughout this study, we assume a standard cosmology with $\Omega_{\rm m} = 0.27$, $\Lambda = 0.73$ and $H_o = 71$ km s^{-1} Mpc^{-1}.

2 THE SAMPLE

2.1 Sample selection and observation

This sample was drawn from the *ROSAT*-selected BCS (Ebeling et al. 1998) and the ESO X-ray Cluster Elliptical Spectral Survey (EXCESS) which provided long slit spectra of 201 and 446 BCGs, respectively. The EXCESS spectra were then used to identify clusters with optical line emission, the Hα emission line was identified in 30 per cent of the sample which is consistent with the findings from the BCS (Crawford et al. 1999).

Only objects with an integrated Hα emission greater than 1×10^{-15} erg cm^{-2} s^{-1} were selected. The second selection criteria was that the Hα emission showed an extent greater than 2 arcsec in the long slit observations to ensure only objects with line emission extended on scales greater than the expected seeing were observed.

The VIMOS instrument on the 8.2-m VLT was the primary optical IFU used throughout this work. The IFU is made up of 6400 fibres with a scale on the sky which can vary from 0.33 to 0.67 arcsec per fibre corresponding to a field of view ranging from 13 arcsec × 13 arcsec to 54 arcsec × 54 arcsec. It consists of four arms which split the field of view into four identically sized quadrants. Each quadrant feeds to a separate grism which disperses the incident light on to its own CCD. There are six grisms equipped on each arm which provide overlapping coverage from 360 to 1000 nm with a spectral resolution ranging from $R \sim 200$ to 2500. Due to being located in the Southern hemisphere, potential VIMOS targets

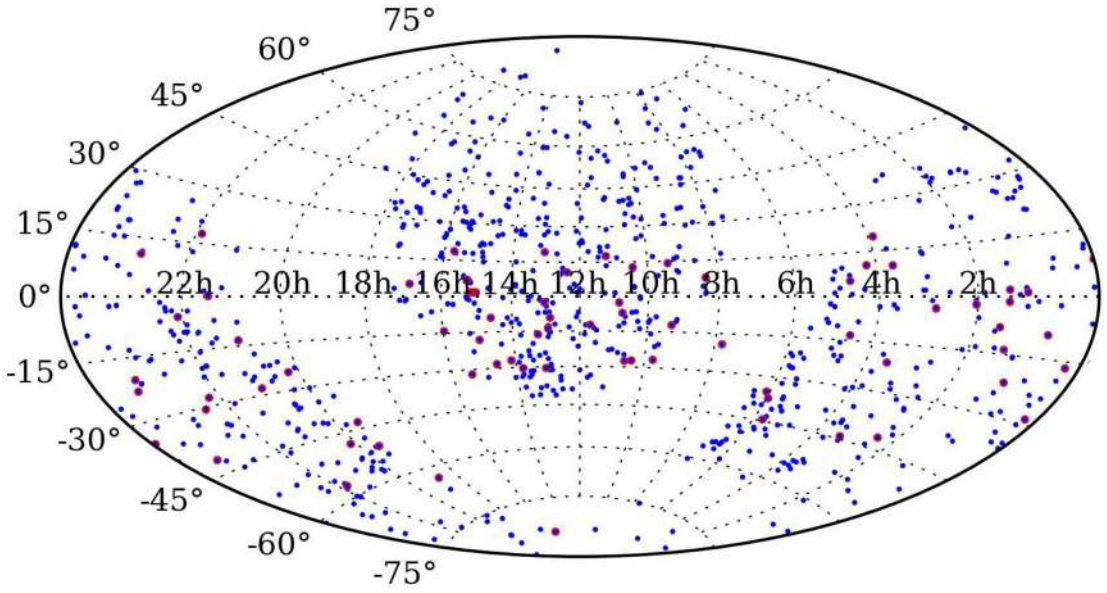

Figure 1. Here we show a plot of the sky identifying the locations of the sample. The blue points show the objects in both the BCS and EXCESS samples, the objects selected and observed with VIMOS are show as larger points, circled in red.

are limited to equatorial southern objects (those with a declination of $<+20$).

The wavelength coverage allows easy access to the bright Hα line in BCGs out to a redshift of $z = 0.25$, while the field of view is more than sufficient to contain the emission in all but the most local clusters. 78 objects matched the selection criteria of which 5 already had optical IFU observations. The final X-ray-selected sample includes all extended Hα bright BCGs out to a redshift $z = 0.25$ and represents an increase in the number of systems studied with IFUs of more than a factor of 5. The presence of extended line emission suggests that all objects in the sample have low central entropy values (Cavagnolo et al. 2008) and are thus consistent with rapidly cooling cores. Fig. 1 shows the locations of all objects from the parent samples and identifies those which were selected to be observed with VIMOS.

At high spectral resolution, the kinematics of the gas can be mapped to a high degree of accuracy with each spectral resolution element (0.6 Å) corresponding to $\sim$30 km s^{-1} (at the wavelengths observed) with broad resolved lines allowing accurate centroiding to a fraction of this. The spectral resolution also allows for the independent fitting of the Hα and [N II] lines meaning a measure of the ionization state of the gas can be obtained from the line ratios. The wavelength coverage also allows for a detection of other important spectral features should they be present including the [S II] doublet (allowing for a measure of the electron density), the sodium D absorption feature (which can be used to study the stellar component of the BCG) and the Hβ and [O III] lines in some objects.

VIMOS was used to obtain optical IFU spectroscopy of the 73 BCGs in the sample between 2007 October and 2008 September. For each object, a set of three 600 s exposures were performed with a pointing dither of 1.5 arcsec included between each to account for bad pixels. The *HR_Orange Grism* and *GG435* filter (spectral resolution of $\sim \lambda/\Delta\lambda \sim 2650$ over a wavelength range 5250–7400 Å) were used to observe Hα($\lambda_{\rm rest}$6562.8 Å) in clusters with a redshift below 0.13. For clusters with a redshift greater than this, the *HR_Red Grism* and *GG475* filter (spectral resolution of $\sim \lambda/\Delta\lambda \sim 3100$ over a wavelength range 6450–8600 Å) were used to sample the Hα. The setup used was selected such that the spectra obtained would cover a spectral range which should include the principle lines of Hα, [O I], [N II] and [S II] assuming they are present in each objects spectrum. As this project was proposed as a bad weather backup project, the observations were taken in a range of conditions, with a median seeing of $\sim$1.5 arcsec but with a range $\sim$0.5–2.6 arcsec. Both the *HR_Orange* and the *HR_Red* modes offer a 27 arcsec $\times$ 27 arcsec field of view which is covered by 1600 fibres. Each fibre is coupled to a micro-lens to give near-continuous sky coverage with each fibre observing a region of 0.67 arcsec in diameter. Details of the observations are summarized in Table 1.

2.2 Data reduction

The raw data were reduced using the VIMOS specific recipes in the ESO Recipe Execution Tool ESOREX. This package performed the basic data reduction on each data cube (a total of 12 for each object, 1 for each quadrant from the three pointings) including bias subtraction, flat fielding, and the wavelength and flux calibration. The wavelength calibration is achieved by comparing a separate exposure of an arc lamp which produces emission lines at known wavelengths and comparing these observations to a catalogue of known line positions. At each spatial element, the lines are identified and their position compared to that in the catalogue, differences between pixels are then corrected allowing the procedure to account for instrumental distortions. The flux calibration is done using observations of a standard star (one for each quadrant of the IFU) which is compared to a standard spectrum of the star to determine the efficiency and response curves of the spectrograph. A standard extinction table is then used to calculate the flux losses due to the atmosphere at a given airmass at each wavelength, after which the scientific spectrum is multiplied by the response curve to produce the final flux-calibrated spectrum. Differences in the seeing conditions and airmass of the observations and standard star are the main contributing factor affecting the flux calibrations. To minimize these effects, standard stars were observed separately for each object during the observations to minimize these differences. Excluding such systematic errors, the method achieves an accuracy of better than 0.5 per cent. Full details of the data reduction pipeline

Table 1. The observational parameters listed for each object in the VIMOS sample. The first column states the cluster designation as used throughout this paper. The redshift is the median redshift acquired from the fits to the H α–[N II] complex, the median is calculated from the fits after dropping the top and bottom 2.5 per cent of the redshifts. The grating is the VIMOS grating used for the observations and the exposure lists the total integration time on target. The seeing is calculated as the mean of the DIMM seeing across all exposures for each object. Lines detected lists all lines apart from the H α and [N II] lines that were detected by visual inspection, the H α–abs line is included for systems which show some evidence of H α absorption. The right ascension and declination are measured at the centre of the field of view for each observation. X-ray luminosities were taken from the surveys of Böhringer et al. (2004), Ebeling et al. (1998) and Ebeling et al. (2000) and temperatures are taken from Ebeling et al. (1996, 1998, 2000) and Cavagnolo et al. (2009). The classifications are based on the X-ray properties following Bahcall (1999). The full table can be found in Appendix A.

The observational parameters listed for each object in the VIMOS sample										
Cluster	Redshift	Grating	Exposure (s)	Mean Seeing(arcsec)	Lines detected	RA	Dec.	L_x (10^{43} erg s^{-1})	T_x (keV)	Classification
Abell 1060	0.012 63	HR-orange	3×600	0.79		10:36:42.78	−27:31:39.66	3.34	3.2	Cluster
Abell 1084	0.133 01	HR-red	3×600	0.68	[O I]	10:44:32.69	−07:04:05.21	48.99	7.3	Cluster
Abell 11	0.149 10	HR-red	3×600	0.77	[O I], [S II]	00:12:33.58	−16:28:05.17	18.2	–	Cluster
Abell 1111	0.165 18	HR-red	3×600	0.85	[O I], [S II]	10:50:36.26	−02:36:13.37	27.30	–	Cluster
Abell 1204	0.170 57	HR-red	3×600	0.81	[O I]	11:13:20.08	17:35:37.88	72.6	3.78	Cluster
Abell 133	0.056 65	HR-orange	3×600	0.93	[O I], [S II]	01:02:41.49	−21:52:48.62	16.17	3.71	Cluster
Abell 1348	0.119 85	HR-orange	3×600	0.87	Hβ, [O III], [N I], [O I]	11:41:24.12	−12:16:35.90	21.09	5.5	Cluster

–

and processes can be found in the VIMOS Pipeline User Manual (VLT-MAN-ESO-19500-3355).

To subtract the sky, point-like objects were masked to remove any stars within the field. Such objects were defined as having a roughly 2D-Gaussian intensity profile with an full width at half-maximum (FWHM) of the order of the seeing and were removed out to the diameter of the seeing. The BCG was then removed by masking all pixels within an isophote of half its peak intensity. Using a lower threshold (40 per cent) had a negligible effect on the sky level (the medium over all sampled spatial elements remained the same to six decimal places) for all but the most local objects (z less than ∼0.01). By contrast, choosing a higher threshold (60 per cent) resulted in a median increase in the sky level across all objects of 3 per cent suggesting that sufficient light from the BCG is being sampled to affect the sky measurement. Thus, the 50 per cent level was chosen empirically as the best compromise to allow a good sampling of sky pixels while removing the majority of the BCGs light. The small field of view means that objects other than the BCG, which are not point-like, were rare in our sample, however, some observations did contain them. These objects where removed in the same way as the BCG, using the same threshold and their peak intensity to produce the mask. The sky level for each quadrant was calculated by taking the median value of the remaining pixels at each wavelength increment. The sky spectrum was subtracted from each pixel in the four quadrants before they were combined into a single data cube.

For low-redshift objects ($z \lesssim 0.02$), the BCG easily fills a single quadrant, so a higher flux threshold for removing the BCG must be used which can result in a substantial oversubtraction of the sky. For such objects, subtraction of a straight continuum baseline prior to the sky subtraction proved a more reliable means of isolating the emission lines. The continuum baseline was calculated from the spectrum at each spatial resolution element by taking the median of the emission either side of the lines of interest. The spectral range used to calculate the median was 120 Å in length and began 60 Å from the emission line on either side. The continuum baseline was then produced by interpolating over the wavelength range to be fitted between the medians calculated at either side of the emission lines. Once this baseline had been subtracted, the sky was subtracted in the same manner as the higher redshift objects before the lines are fit. The drawbacks of this method, however, are that it is only valid for a small spectral range, so only one line complex can be studied in a given reduction and it also eliminates any information carried in the objects continuum emission.

Finally, the three exposures were median combined for each pointing in order to eliminate cosmic rays. The exception to this was RXCJ2014.8-2430 which only had two pointings, so the mean of the two observations was used to produce the final cube. The final mosaics provided cubes with a ∼30 arcsec × 30 arcsec field of view once the dithering offsets are taken into account.

2.3 IFU data cube analysis

We took the IFU data cubes produced by the reduction and fit spectral models to the key lines at each resolution element. The primary diagnostic line structure was the H α ($\lambda_{\rm rest}$ 6562.8 Å) and [N II] ($\lambda_{\rm rest}$ 6548.1/6583 Å) complex.

To fit these lines, we extracted a region of the spectrum in each resolution element (lenslet) that was 240 spectral resolution elements in length (∼144 Å) centred at the wavelength of the H α line at the cluster redshift. We then fitted Gaussian emission line profiles to these extracted regions using a χ^2 minimization procedure. To the H α–[N II] triplet of lines, we fit three separate Gaussian profiles on top of a flat baseline to account for variations in the average continuum flux and compare this to just a flat continuum baseline fit (Fig. 2). Each of the three emission line had the form

$$\mathrm{F}(\lambda) = \frac{\mathrm{F}_0}{2\pi\sigma} \times \mathrm{e}^{\frac{-0.5(\lambda-\lambda_z)^2}{\sigma^2}}, \quad (1)$$

with F_0 the total flux in the line, σ the velocity dispersion of the line (FWHM/2(2ln2)$^{0.5}$), λ the wavelength at a given position and λ_z the wavelength of the line corrected for redshift. The model spectrum contains three such lines with fixed (at redshift 0) separations, the H α–[N II]$_{\lambda6583/\lambda6548.1}$ triplet. Each line was produced independently and the resulting spectral models where added together on top of a flat baseline to produce the final spectral model.

The fitting routine was given an array of first guess variables which were then used to produce the fit. For the H α–[N II] triplet, these variables were as follows

(i) The redshift of the emission: the redshift was used to determine the value of λ_z in equation (1), such that $\lambda_z = \lambda_0 \times (1 + z)$.

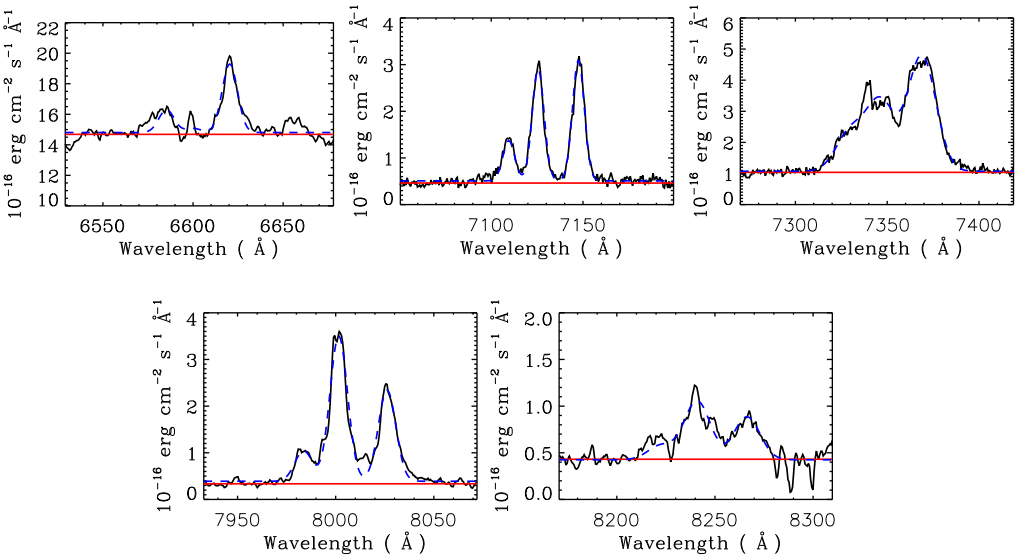

Figure 2. Here we show several spectra showing the Hα and [N II] lines which represent the sample. The spectra are of the central region of five objects and the wavelength coverage is the same as the region used by the fitting routine. From left to right, top to bottom: the redshifts of the objects are ≈0 (NGC 5846), ≈0.08 (Abell 478), ≈0.13 (Abell 1348), ≈0.21 (Abell 3017) and ≈0.26 (Abell 3444) so they are the representative of the whole sample. The red solid line shows the flat continuum baseline fit and the blue dashed line shows the best-fitting spectral model. The variation of flux, [N II]/Hα ratio and linewidth are apparent from these plots.

Where λ_0 is the rest wavelength of the line and z is the redshift. The first guess for the redshift at each position was set to the systemic redshift of the BCG.

(ii) The total flux in the Hα line. This was used as F_0 for the Hα line in equation (1). The first guess was set to the average flux at the wavelength of the line across the whole cube.

(iii) The total flux in the $[N\,II]_{\lambda6583}$ line. This was used as F_0 for the $[N\,II]_{\lambda6583}$ line in equation (1), F_0 for the $[N\,II]_{\lambda6548.1}$ line was fixed at one-third of this value. The first guess was set to be equal to the Hα flux.

(iv) The FWHM of the line in angstroms: this was used to calculate σ in equation (1), such that $\sigma = \mathrm{FWHM}/2(2\ln2)^{0.5}$. The first guess set to the width of a skyline, ∼4.7 Å.

(v) The baseline flux level: this was not used to produce any of the three line models but was added to the total model spectrum after they had been produced to account for variations in the median level of the continuum between lenslets.

The redshift and width of the [N II] and Hα lines were set to be the same to reduce the number of free parameters in the model. After producing the first guess the redshift, Hα flux, $[N\,II]_{\lambda6583}$ flux, linewidth and continuum baseline level were allowed to vary using a least-squared fitting routine (Moré & Wright 1993) until the model minimized to best fit the data. During the minimization, the parameters were constrained to ensure only the emission lines of interest were recovered and reduce the processing time required to achieve a fit. We constrained the Hα and $[N\,II]_{\lambda6583}$ flux to positive values (emission) and the sigma linewidth to $<$1000 km s^{-1} (FWHM∼2355 km s^{-1}). These profiles were initially fitted to the spectrum from each 0.67 arcsec lenslet and adaptively binned to ∼2.0 arcsec (3 × 3 lenslets) in regions with lower Hα flux, as such the fits to the low-surface brightness emission have a lower spatial resolution than the brightest regions.

We accepted these fits as representing the presence of spectral lines in the data when they provided an improvement in signal to noise (S/N) of 7 (seven times the standard deviation, or 7σ) when compared to a continuum baseline only fit. When an acceptable fit was found, the parameters of the best-fitting model were stored and the 1σ errors were calculated by varying each parameter slightly from the best fit and allowing all others to re–minimize. For each pixel where an acceptable fit was found, we attempted to fit a second model which included an additional line component with a redshift, intensity and width independent of the initial fit. This extra component was allowed to become much broader than the initial fit (it was left unconstrained) and was included as a means to test the spectra for additional velocity components and broad-line features. This model was then accepted when it provided an improvement in S/N of 15 (15 times the standard deviation, or 15σ) when compared to a continuum baseline only fit. For pixels where a second component was found to be significant a model including a second component for all lines was fitted to the data and the errors were recalculated to account for the new model. This process detected only two objects with multiple velocity components and eight with broad components in their core regions. As multiple velocity components do not make up a significant fraction of the sample we choose not to address the nature and origin of the additional components in this paper. The significance of these models was tested on a number of objects using an F–test of additional parameters. The basic Hα–[N II] line model when compared to a baseline only model was found to always have a significance level of $\alpha < 0.001$ when required to fit a S/N of 7σ. Likewise, the threshold of a S/N of 15σ was selected, so as the additional line components had a significance level of $\alpha < 0.001$ when compared to the standard Hα–[N II] line model.

The parameters of the fits were then used to produce maps of the line flux, line-of-sight velocity and FWHM deconvolved for instrumental resolution. The velocity zero-point was determined as the median of the measured velocities after removing the highest 2.5 per cent and lowest 2.5 per cent of the values. A retrospective clipping method was used to remove pixels in which the fitting routine had returned parameters with non-physical properties

(velocities in excess of $\pm$1000 km s^{-1} relative to the mean which are unlikely to be associated with the BCG). Continuum images of the region covered by the observations were produced by taking the median from each lenslet over a region of the spectra (hereafter, referred to as collapsing the cube) containing no emission lines or sky line residuals. These were produced to allow comparison between the position of continuum objects and the structure of the Hα emission to identify possible offset peaks (Hamer et al. 2012) or interactions with other cluster members.

2.4 Observational parameters

Table 1 outlines the key observational parameters of each object in the sample. The redshift quoted in Table 1 is the median redshift of the Hα line in the object. Most of the objects in the sample had all pointings performed on the same day, or at least in similar conditions. However, RXCJ2014.8-2430 had one of its pointings performed in very poor conditions. As such, we have only used two of the pointings to make the final cube. RXCJ2101.8-2802 had pointings which were taken on different days, with four pointings in total, all of which were in consistent conditions and showed no other problems in the spectra, so we choose to use all four pointings, giving this object a slightly longer integration time. We calculated the mean seeing of all observations to be $\sim$1.5 arcsec. Before the full fitting routine was run on an object, its spectrum was studied to identify the presence of additional emission lines (lines other than Hα and [N II]), these additional lines are listed in Table 1. We base our classifications on the X-ray properties of each object (X-ray luminosity and where available, X-ray temperature) using the classification of Bahcall (1999) (Groups $< L_x = 10^{43}$ erg s$^{-1} <$ Clusters and Groups $< T_x = 2$ keV $<$ Clusters). By this definition, our sample consists of 61 brightest cluster galaxies and 12 brightest group galaxies.

3 THE RAW DATA: CHANNEL MAPS

We begin by presenting channel maps of several representative objects produced from the fully analysed data cubes which show the Hα emission at different velocities. To produce the channel maps, we baseline-subtracted each spatial resolution element by fitting a straight line to the spectrum. This was then subtracted to remove the bulk of the continuum emission from the cube. Channels at greater than $\pm$1000 km s^{-1} relative to the redshift of the BCG were then used to determine the average continuum-subtracted channel noise of the observation, these channels were then discarded. The remaining channels contained the Hα emission from the cluster core. For channels where the continuum subtracted emission exceeds seven times the average continuum-subtracted noise, a flux map was produced to show the location of the Hα emission in that channel. Each map gives the velocity of its channel with respect to the median velocity of the Hα emission for that object. For reference, the centre of the continuum emission from the BCG for each object is marked on its respective maps with a green cross. This position was determined by fitting two-dimensional Gaussian profiles to a collapsed continuum image.

We first show the channel map of Hydra-A (Fig. 3) which shows evidence for a rapidly rotating disc within its core (Hamer et al. 2014). This is apparent from the channel maps which show a shift in the position of the bright component of the Hα emission as the velocity changes. Additionally, we see that the filaments extending to the north and south also show a velocity shift, with the northern filament being slightly blueward of the core and the southern filament shifted towards the red. This velocity shift is not clearly apparent in the velocity map displayed in Hamer et al. (2014) as the shift is small relative to the total velocity shift in the system. This kind of velocity structure, with a shift in the velocity of the bulk of the emission across the BCG, is common amongst the objects in the sample clearly visible in the channel maps of 31/73 clusters. The velocity shift in most is not as extreme as that seen in Hydra-A, however, this is not surprising given we are viewing the disc in Hydra-A at close to edge-on (Hamer et al. 2014).

NGC 5044 has narrow-band imaging that shows an extensive network or Hα filaments (Werner et al. 2014) similar to those seen in the archetype cooling flow NGC 1275. Our VIMOS observations do not resolve the individual filaments but do indicate diffuse extended emission to the south in the region where the filaments are found. We see this emission extending to the south in channels close to the BCGs central velocity (Fig. 3). The kinematics correlate well with those of the molecular CO(2–1) emission seen by David et al. (2014), in the centre the line profile is broad (FWHM $\sim$ 400–500 km s^{-1}) and double-peaked suggesting two velocity components separated by $\sim$300 km s^{-1} are present. Multiple velocity components such as this are only apparent in the channel maps of NGC 5044. However, they have been observed in IFU observations of other systems (e.g. Abell 1664; Wilman, Edge & Swinbank 2006, 2009) warranting a more detailed search for their presence. The channel maps of NGC 5044 show that the brightest region of the emission can be found at different positions within the BCG at different velocities. It is slightly extended towards the north-west at velocities blueward of the BCG (< -200 km s^{-1}), runs from the north-east to south-west of the BCG at ~ -120–0 km s^{-1} and extends slightly to the south-east when redward of the BCG (>150 km s^{-1}) suggesting that it has no ordered velocity structure. This redshifted region matches the position and velocity relative to the centre of the system of GMA 18 identified in David et al. (2014). Low-surface brightness extended regions of Hα emission similar to those seen in NGC 5044 are seen in 9/73 objects in our sample suggesting that while other filamentary structures may be present in our sample, they are not common. The channel maps for all objects can be seen in Appendix B.

It is clear from the channel maps that there is a wide variety of morphologies of the Hα-emitting gas between objects. Some objects appear very compact from their Hα emission while others are very extended. Some of this results naturally from the variation in redshift of the objects within the sample, however, there remains a large variation when we consider the a physical extent of the objects (See Table 2).

In addition to their varied spatial morphology, many systems show a significant, coherent velocity gradient across the BCG (31/73). This suggests the presence of an ordered velocity field within the gas which, for one object (Hydra-A) we know, traces a rotating disc of gas that aligns with the radio and X-ray structure in the system (Hamer et al. 2014). The presence of such a velocity structure in a large fraction of BCGs would have important implications for our understanding of cluster cores.

4 THE STRUCTURE AND KINEMATICS OF THE GAS

In order to parametrize the data and make it easier to analyse, we fit Gaussian emission line profiles to the Hα and [N II] lines in each lenslet (see Section 2.3) We now study the maps of these

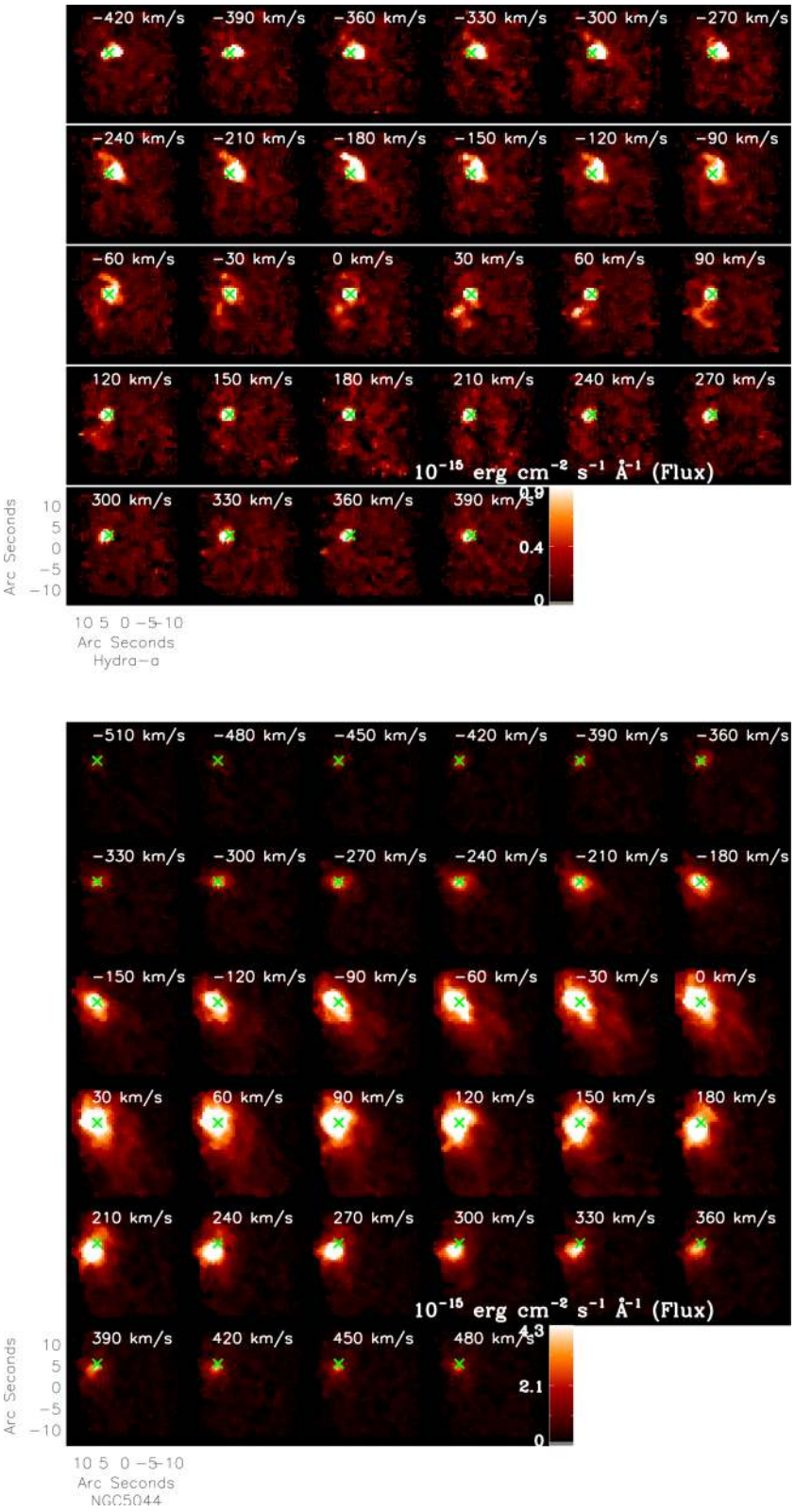

Figure 3. Top – here we display continuum subtracted maps of the H α emission in Hydra-A for each channel containing emission. Each map gives the velocity of its channel with respect to the median velocity of the H α emission. The green cross marks the centre of the continuum emission from the BCG. The maps clearly show a shift in the centroid of the H α emission as the velocity changes which follows the disc within this object. Bottom – the channel maps of NGC 5044 showing the H α emission in velocity slices. The green cross marks the centre of the continuum emission from the BCG. These maps show a low-surface brightness region of extended diffuse emission to the south where filaments are seen in narrow-band images. The core region of the emission shows a chaotic variation in structure between velocity channels suggesting the kinematics in the core are quite complex and disturbed. Channel maps for every object can be found in Appendix B.

Table 2. Here we list the derived parameters for every object from the sample. The velocity column refers to the peak-to-peak velocity measured across the mean line-of-sight velocity map. The extent is the length of the major axis. The luminosity is calculated only for flux that appears at greater than 7σ significance. The FWHM is measured from the spectrum of the central $\sim$2 arcsec $\times$ 2 arcsec.

	The derived parameters listed for each object in the VIMOS sample					
Cluster	Velocity (km s^{-1})	Extent kpc (arcsec)	$L_{H\alpha}$ (10^{40} erg s^{-1})	FWHM (km s^{-1})	[N II]/H α	Morphology
Abell 1060	68 ± 11	1.22(4.73)	0.043 ± 0.0086	107 ± 17	0.7 ± 0.3	Quiescent
Abell 1084	269 ± 30	11.23(4.75)	11 ± 1.8	275 ± 108	0.9 ± 0.5	Quiescent
Abell 11	247 ± 15	29.58(11.37)	70 ± 6.5	340 ± 61	0.9 ± 0.5	Quiescent
Abell 1111	478 ± 22	21.94(7.75)	33 ± 3.9	297 ± 75	1.1 ± 0.5	Plume
Abell 1204	490 ± 29	26.32(7.15)	59 ± 5.4	514 ± 355	1.7 ± 0.6	Disturbed
Abell 133	210 ± 32	7.18(6.53)	1.2 ± 0.16	308 ± 14	1.7 ± 0.2	Plume
Abell 1348	755 ± 40	18.05(8.35)	46 ± 6.3	513 ± 153	1.6 ± 0.5	Quiescent
Abell 1663	225 ± 45	13.71(8.66)	1.7 ± 0.29	526 ± 120	3.4 ± 0.4	Quiescent/compact
Abell 1668	302 ± 22	10.90(8.92)	4.7 ± 0.45	339 ± 28	2.2 ± 0.7	Quiescent
Abell 194	85 ± 7	1.49(4.03)	0.50 ± 0.071	211 ± 122	0.8 ± 0.23	Compact
Abell 1991	124 ± 10	16.41(14.38)	4.0 ± 0.35	209 ± 64	1.5 ± 0.3	Offset
Abell 2052	268 ± 18	6.44(9.41)	1.8 ± 0.18	454 ± 105	2.2 ± 1.1	Disturbed
Abell 2390	490 ± 29	25.99(7.06)	109 ± 15	422 ± 52	0.95 ± 0.48	Quiescent
Abell 2415	186 ± 37	11.25(10.08)	4.5 ± 0.42	275 ± 180	1.5 ± 0.55	Plume
Abell 2495	201 ± 16	8.88(5.93)	0.56 ± 0.090	235 ± 38	1.5 ± 0.074	Quiescent
Abell 2566	325 ± 22	10.18(6.5)	9.7 ± 1.2	172 ± 74	0.91 ± 0.56	Offset
Abell 2580	203 ± 24	9.40(5.71)	2.4 ± 0.48	340 ± 157	0.75 ± 0.55	Compact/plume
Abell 2734	210 ± 20	6.09(5.09)	1.1 ± 0.27	551 ± 105	2.5 ± 1.0	Quiescent
Abell 291	294 ± 70	23.14(7.12)	480 ± 31	626 ± 371	0.99 ± 0.55	Disturbed
Abell 3017	390 ± 31	25.03(7.06)	110 ± 17	366 ± 106	0.62 ± 0.33	Quiescent
Abell 3112	225 ± 19	8.94(6.20)	7.1 ± 1.3	893 ± 256	1.9 ± 1.2	Quiescent
Abell 3378	106 ± 15	20.63(8.30)	6.1 ± 0.95	422 ± 170	1.1 ± 0.39	Quiescent(filament)
Abell 3444	428 ± 41	35.70(8.99)	66 ± 10	394 ± 140	0.67 ± 0.54	Offset
Abell 3574	161 ± 15	1.53(5.32)	0.88 ± 0.061	82 ± 16	0.56 ± 0.37	Disturbed
Abell 3581	464 ± 19	5.43(12.44)	2.4 ± 0.14	379 ± 69	1.6 ± 1.0	Disturbed
Abell 3605	269 ± 20	7.37(5.96)	4.5 ± 0.72	484 ± 130	2.4 ± 1.0	Quiescent
Abell 3638	111 ± 19	8.61(5.91)	5.9 ± 0.90	403 ± 67	1.3 ± 0.97	Quiescent
Abell 3639	150 ± 58	18.79(7.16)	56 ± 4.5	367 ± 73	1.4 ± 0.56	Quiescent
Abell 3806	136 ± 14	5.90(4.16)	3.3 ± 0.69	231 ± 52	2.9 ± 0.88	Quiescent
Abell 383	181 ± 52	24.25(7.69)	40 ± 5.0	386 ± 73	1.5 ± 0.64	Plume
Abell 3880	444 ± 20	13.24(11.72)	12 ± 0.89	438 ± 50	1.8 ± 0.95	Plume
Abell 3998	346 ± 66	17.85(10.61)	7.5 ± 0.57	253 ± 137	1.4 ± 0.18	Plume(filament)
Abell 4059	396 ± 46	7.89(8.22)	4.1 ± 0.48	536 ± 97	2.5 ± 2.0	Quiescent
Abell 478	176 ± 12	17.04(10.62)	23 ± 2.3	261 ± 32	1.1 ± 0.92	Quiescent
Abell 496	252 ± 8	8.19(12.46)	3.1 ± 0.28	260 ± 46	2.1 ± 1.3	Quiescent
Abell 795	315 ± 38	11.13(4.66)	18 ± 3.7	755 ± 64	1.5 ± 0.85	Quiescent
Abell 85	217 ± 29	8.31(7.74)	1.6 ± 0.20	339 ± 54	2.3 ± 0.47	Quiescent(filament)
HCG62	168 ± 12	3.30(11.38)	0.087 ± 0.011	204 ± 101	3.0 ± 0.53	Quiescent
Hydra-A	556 ± 6	7.95(7.68)	13 ± 1.7	346 ± 58	0.86 ± 0.56	Quiescent
NGC4325	255 ± 10	6.66(12.98)	0.90 ± 0.089	236 ± 34	1.5 ± 0.59	Disturbed
NGC5044	277 ± 18	5.60(30.51)	0.54 ± 0.062	457 ± 99	2.5 ± 0.65	Disturbed
NGC533	211 ± 19	2.77(7.14)	0.19 ± 0.033	376 ± 218	3.1 ± 1.4	Quiescent
NGC5813	223 ± 24	1.48(10.61)	0.044 ± 0.0059	503 ± 81	2.1 ± 0.63	Disturbed
NGC5846	117 ± 12	1.27(10.12)	0.076 ± 0.0056	255 ± 63	3.0 ± 0.88	Quiescent
RXCJ0120.9-1351	345 ± 8	4.66(4.71)	1.5 ± 0.28	361 ± 40	2.2 ± 1.3	Quiescent(filament)
RXCJ0132.6-0804	452 ± 16	24.78(9.57)	43 ± 5.7	434 ± 66	1.5 ± 0.66	Quiescent
RXCJ0331.1-2100	125 ± 38	14.47(4.51)	54 ± 7.6	592 ± 184	1.2 ± 1.0	Quiescent
RXCJ0543.4-4430	245 ± 53	12.97(4.61)	4.7 ± 0.98	259 ± 169	1.9 ± 0.35	Quiescent
RXCJ0944.6-2633	289 ± 8	25.54(10.19)	36 ± 4.4	277 ± 132	0.58 ± 0.40	Disturbed
RXCJ1257.1-1339	468 ± 17	6.82(22.74)	1.4 ± 0.087	274 ± 116	1.1 ± 1.0	Quiescent
RXCJ1304.2-3030	343 ± 17	3.33(14.87)	1.2 ± 0.072	375 ± 41	1.5 ± 0.9	Quiescent(filament)
RXCJ1436.8-0900	199 ± 16	14.57(9.55)	14 ± 1.7	273 ± 14	1.4 ± 1.0	Quiescent
RXCJ1511.5+0145	138 ± 45	5.03(6.38)	0.29 ± 0.062	553 ± 113	3.0 ± 0.40	Quiescent
RXCJ1524.2-3154	310 ± 19	15.57(8.30)	46 ± 3.9	492 ± 47	1.3 ± 1.2	Plume
RXCJ1539.5-8335	333 ± 59	13.74(9.59)	30 ± 2.0	572 ± 123	1.1 ± 0.56	Disturbed
RXCJ1558.3-1410	275 ± 28	13.82(7.71)	22 ± 2.6	465 ± 103	1.2 ± 0.71	Quiescent
RXCJ2014.8-2430	539 ± 13	18.60(6.92)	140 ± 12	462 ± 92	0.78 ± 0.55	Quiescent
RXCJ2101.8-2802	169 ± 10	7.16(10.76)	1.0 ± 0.11	106 ± 17	0.54 ± 0.32	Offset
RXCJ2129.6+0005	157 ± 29	30.53(8.20)	32 ± 4.6	314 ± 64	0.93 ± 0.32	Quiescent
RXCJ2213.0-2753	185 ± 17	32.25(2.72)	0.92 ± 0.32	660 ± 372	1.4 ± 1.1	Compact/quiescent

Table 2 – *continued*

Cluster	Velocity (km s^{-1})	Extent kpc (arcsec)	$L_{H\alpha}$ (10^{40} erg s^{-1})	FWHM (km s^{-1})	[N II]/H α	Morphology
RXJ0000.1+0816	128 ± 3	3.55(4.57)	1.9 ± 0.17	388 ± 74	1.7 ± 0.57	Disturbed
RXJ0338+09	388 ± 6	8.60(12.54)	8.3 ± 0.50	327 ± 77	1.1 ± 0.96	Disturbed
RXJ0352.9+1941	244 ± 19	17.81(9.0)	62 ± 5.3	551 ± 45	0.79 ± 0.64	Quiescent
RXJ0439.0+0520	236 ± 54	26.15(7.70)	62 ± 7.1	559 ± 92		Quiescent
RXJ0747-19	354 ± 32	24.76(13.11)	63 ± 6.1	422 ± 83	1.7 ± 0.77	Disturbed
RXJ0821+07	270 ± 20	20.44(10.12)	35 ± 3.7	180 ± 49	0.84 ± 0.49	Plume
RXJ1651.1+0459	309 ± 25	17.50(6.52)	29 ± 4.0	276 ± 152	0.54 ± 0.39	Quiescent
S555	287 ± 20	11.54(13.08)	4.5 ± 0.44	578 ± 234	1.8 ± 1.1	Quiescent
S780	420 ± 17	33.04(8.87)	240 ± 28	490 ± 49	1.1 ± 0.95	Plume
S805	141 ± 22	2.75(8.91)	0.18 ± 0.018	227 ± 59	3.7 ± 0.95	Quiescent(filament)
S851	523 ± 17	3.58(18.56)	0.53 ± 0.039	425 ± 71	3.5 ± 3.1	Quiescent
Z3179	278 ± 15	14.80(5.92)	7.6 ± 1.5	482 ± 82	2.3 ± 0.97	Quiescent
Z348	226 ± 12	42.02(10.66)	390 ± 48	508 ± 71	0.57 ± 0.49	Quiescent

parametrized fits to the H α and [N II] triplet for all 73 objects in our sample. Five panels were produced for each object showing the continuum emission, the H α flux map, the ratio of the [N II] to H α, the line-of-sight velocity field and the FWHM. It should be noted that in some systems where the continuum is very high and H α flux is low, not all of the H α is recovered due to the underlying absorption feature caused by H α in stellar atmospheres. In such cases, the H α line often appears very weak or even completely absent from some parts of the cube where it is otherwise expected to be (such as regions were the other ionized lines are strong). Systems with this problem were typically of low redshift and thus filled much of the field of view making producing an empirical model of the absorption from a bright region of the galaxy devoid of line emission difficult or impossible.

Rather than trying to model out the absorption as a component of the fitting routine (which would have reduced the degrees of freedom for these objects), we fitted the spectrum as normal. In these cases, the spectral fit was primarily constrained by the bright [N II](λ_{rest} 6583 Å) line which could introduce some bias as the two lines may be tracing different excitation mechanisms (AGN processes typically produce more [N II] for a given H α than star formation, for example). However, in all such cases, the [N II]/H α ratio is high so [N II] provides a higher significance tracer of the gas dynamics without the degeneracy of additional model parameters needed to model out the absorption. In such cases, the maps show the [N II] flux rather than the H α.

To determine the effect of the bias introduced by this approach, we produced maps constrained only by the [N II] for systems where H α and [N II] were equal in strength and compared them to the H α-constrained maps. We found no significant difference between the maps suggesting that the [N II] emission is tracing the same morphology and kinematics as the H α, at least in the case of the galaxies, we could perform this test on. We adopt the assumption that this concordance extends to objects for which H α emission was too weak and the stellar absorption component dominates to produce reliable maps constrained by H α. Fig. 4 shows maps of the parametrized fits for a sub-sample of objects, the maps of the full sample are available in Appendix C.

4.1 H α morphology

From the maps shown in Fig. 4, we can calculate the extent of the line-emitting region for each object. We define the major axis to be the maximum length of continuous emission (at greater than 7σ) along a line through the peak of the H α emission (throughout this paper, we use extent and major axis interchangeably). The minor axis is then the length of continuous emission perpendicular to the major axis (also through the peak of the H α). This definition assumes that the distribution of H α emission is well approximated by an ellipse. This is clearly not the case for all objects in the sample, though, it is a good approximation to regions of uniform H α distribution in most systems. We note, however, that it is also important to characterize the overall distribution of the emission for those objects which are extended.

As can be seen from Fig. 4, the H α morphology varies greatly from system to system. We categorize these morphologies into five distinct groups. It is important to note that the definitions are not all mutually exclusive, as such it is possible that a single object may exhibit a morphology which is consistent with two or more of the definitions given below.

Compact objects: compact objects are defined as objects in which the minor extent of the H α emission above a significance of 7σ is less than twice the mean of the Differential Image Motion Monitor (DIMM) seeing during the observation of that object. The selection criteria of the VIMOS sample required that every object has an extent of more than 2 arcsec in the FOcal Reducer and low dispersion Spectrograph (FORS) spectra. As such very few objects should fall into this definition, however, we include it to account for observations taken in very poor seeing conditions. It is important to note that this definition of compact makes no consideration of the physical scale of the objects. However, it is an important classification as any apparent spatial variations along the minor axis seen for such objects cannot be believed. Objects that are given this classification are also classified according to the structure seen along their major axis unless this too is less than twice the seeing.

Plumes: an object is classified as having a plume when the H α emission shows a clear extent in one preferential direction which is not shared by the continuum emission. Typically with this type of object, the bright central region of the H α emission also shares the shape of the larger scale plume which results in the peak of the H α emission being slightly offset from the peak in the continuum. This offset is never a large physical separation ($\lesssim$7 kpc) but is an important parameter to distinguish plumes from quiescent objects in which H α emission is only detected to one side of the BCG, the latter showing no offset larger than the mean seeing.

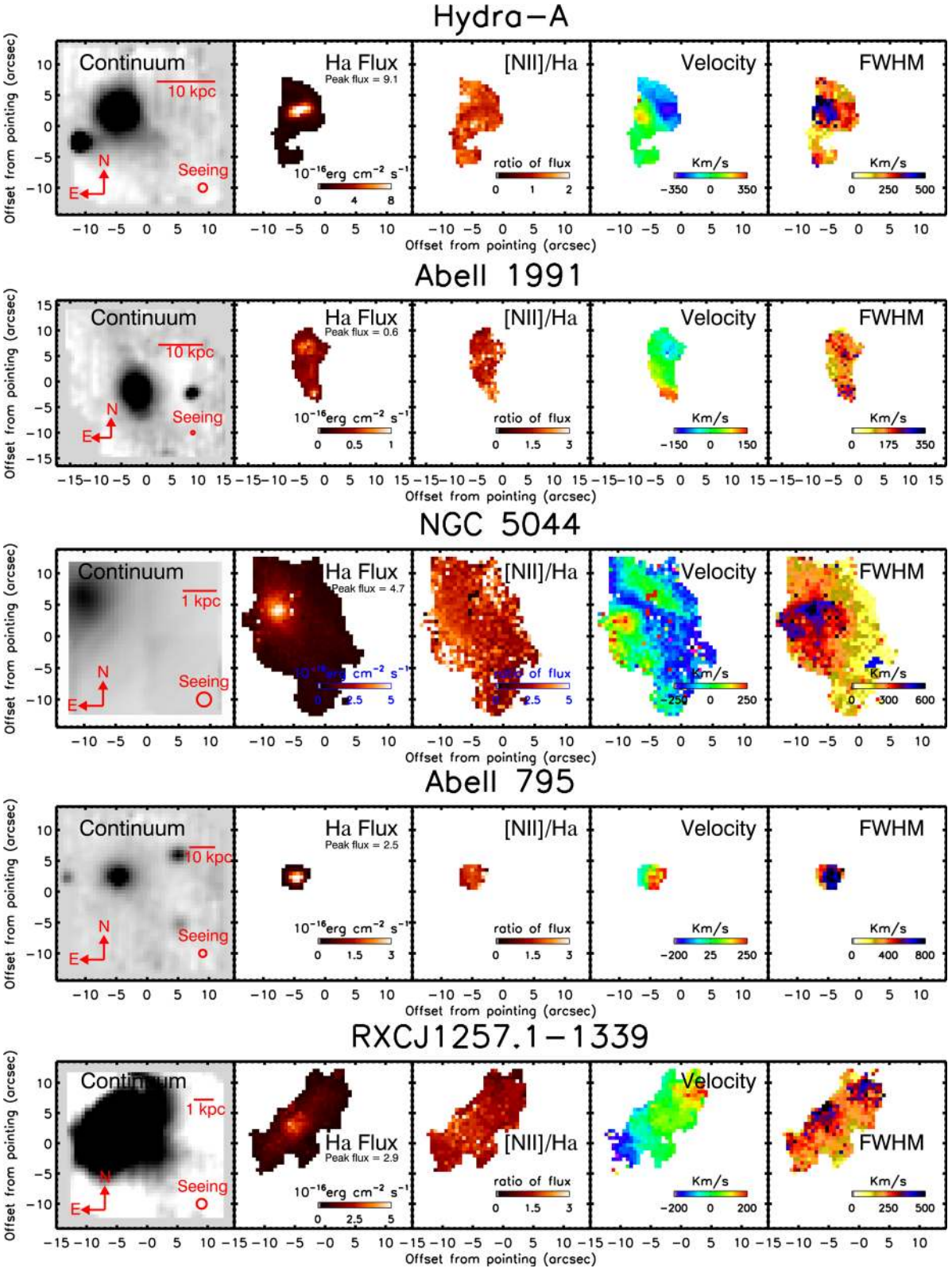

Figure 4. Maps of the spectral fits to the VIMOS data cubes for the five objects from the sample. From left to right the panels are: (1) a continuum image created by collapsing the cube over a wavelength range free of emission and sky lines, (2) The H α flux map, (3) a map showing the ratio of [N II] to H α flux, (4) the line-of-sight velocity profile of the H α and [N II] emission, (5) the full width at half-maximum (FWHM) of the emission line deconvolved for instrumental resolution.

Offset objects: objects classified as offset show a Hα morphology in which either all of the emission is offset from the peak of the continuum or that have a second Hα peak which contains the majority (>50 per cent) of the Hα flux that is substantially offset from the BCG (> 8 kpc, the maximum physical extent of the seeing in any object from the sample). Although we classify both of these definitions as offset, they show distinctly different Hα morphologies. The objects which are completely offset from the centre of the BCG appear to be otherwise quite similar to quiescent objects in their morphology. The latter kind, however, appear morphologically more consistent with plumes with a clear extent of the low-surface brightness Hα emission extending in a single preferential direction. However, there are two key differences to plumes. First, the extent seen in the low-surface brightness emission is not shared by a similar structure in the bright emission as is the case with plumes. Secondly, those which are classified as offset have a second peak in the Hα emission which is positioned at the end of the extended region of low-surface brightness emission, away from the BCG. For a more detailed analysis of the nature of objects with this kind of offset emission, see Hamer et al. (2012).

Quiescent objects: objects classified as quiescent have Hα emission which is extended beyond twice the seeing and shows a simple elliptical and centrally concentrated morphology. The peak of the Hα emission must lie within the mean seeing of the peak in the continuum and the Hα flux must fall off uniformly as the continuum does (though not necessarily at the same rate as the continuum). Objects with an Hα morphology of this type are likely to be very relaxed and have had no major events occur recently enough to disturb the gas.

Disturbed objects: the final morphological classification we present are disturbed objects. These are objects where the Hα flux typically peaks close to the peak of the continuum but have lower surface brightness Hα emission which is extended and forms non-uniform structures around the BCG. This classification of object essentially includes all objects which are not classified under one of the previous four categories. The extended and non-uniform nature of the Hα emission in this class of objects suggests that some event has disturbed the cold gas in the core of the cluster causing it to flow away from a uniform distribution. Another possibility is that this emission is tracing the gas being accreted by the system. Some of the objects which fall into this category are systems which are well known to have active AGN which can be seen to be disturbing the ICM (for example, Abell 2052; Blanton et al. 2011). This suggests the possibility that objects which fall into this classification are currently undergoing feedback processes which has resulted in the disturbance of the cold gas reservoir.

The classification assigned to each object in the sample can be found in Table 2. Some care must be taken when considering these classifications (in particular, the distinction between quiescent and disturbed objects) as the surface brightness limits of our objects ranges considerably, from 0.38×10^{34} erg s^{-1} kpc^{-2} to 1.64×10^{37} erg s^{-1} kpc^{-2}. We note, however, that these are extreme examples and the sample has a median surface brightness limit of 3.97×10^{35} erg s^{-1} kpc^{-2} with a median absolute deviation of 3.19×10^{35} erg s^{-1} kpc^{-2}. A histogram of the surface brightness limits grouped by classification can be seen in Fig. 5 . The disturbed objects (listed in Table 2) sample the full range of surface brightness limits ranging from 1.90×10^{34} erg s^{-1} kpc^{-2} to 1.64×10^{37} erg s^{-1} kpc^{-2}. However, the median surface brightness limit of the disturbed objects is 1.03×10^{36} erg s^{-1} kpc^{-2} with a median absolute deviation of 8.22×10^{35} erg s^{-1} kpc^{-2} which does

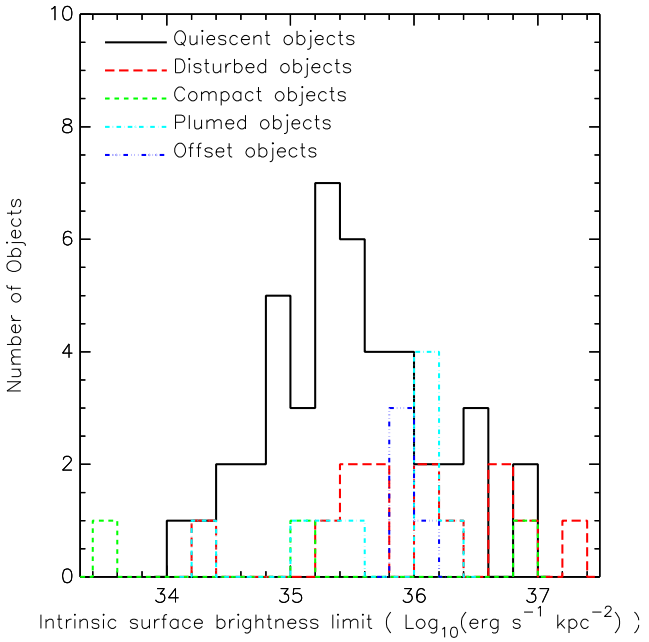

Figure 5. A histogram showing the distribution of intrinsic surface brightness limits for each classification of object. We note that, with the exception of offset objects, all classifications sample the majority of the range of surface brightness limits. Interestingly, the plot does show that 11 out of 14 objects with a surface brightness limit of below 10^{35} erg s^{-1} kpc^{-2} are classified as quiescent suggesting that the higher surface brightness features associated with more complex morphologies can be identified in all systems.

suggest that objects classified as disturbed, typically, have higher surface brightness limits than average for the sample, but is consistent with the median of the full sample within the errors. While the small sample size of disturbed objects (just 13) must be considered when interpreting these values, the large range of surface brightness limits measured for the sample suggest that the surface brightness limit has only a small effect on our ability to distinguish an object's morphology. The seeing of our observations may also play a role in our ability to classify objects correctly, we test this in Fig. 6 by plotting the seeing of the observations against the surface brightness limit for the object. No obvious trends are visible on this plot suggesting that seeing does not have a major impact on our ability to identify an object's morphology. However, we do note that all offset objects where observed in relatively good seeing conditions. This is not unexpected, as a poorer seeing will limit our ability to accurately determine the position of the Hα peak and thus identify the object as offset if the separation is small.

High-resolution narrow-band imaging of Hα in cluster cores has shown the presence of filamentary structures surrounding the BCG. While a few objects in our sample do show narrow filaments of emission which extend out into the ICM, we do not resolve these structures in the majority of cases. Most likely, this is a result of the poorer seeing of our observations smoothing the filamentary structures to such an extent that they appear blended as a continuous region of low-surface brightness emission extended away from the BCG. A good example of this effect is NGC 5044 which is known to have filaments of Hα emission extended to the south-west of the BCG (David et al. 2011). Comparing to our Hα flux map shown in Fig. 4, it is possible to see low-surface brightness emission extended to the south-west over similar distances to the filaments, however, the details of the filamentary structures are not visible in the VIMOS observation. In the few cases where we do see structures which

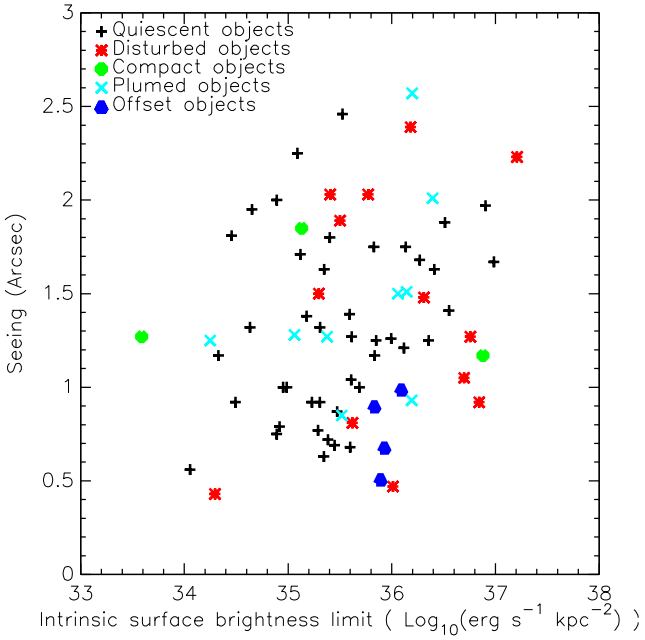

Figure 6. A plot showing the mean seeing of the observations for each object against that objects intrinsic surface brightness limit. Each object is given a different symbol depending on its classification. If the seeing of our observations played a major role in our ability to distinguish the morphology of an object, we would expect to see trends on this plot. However, with the exception of offset objects, all others fill the parameter space with no obvious trends. The offset objects are only seen at good seeing, ∼1 arcsec or below.

appear similar to filaments, we note that their apparent thickness is substantially higher than those observed with narrow-band imaging. While this may be an effect of the seeing, it is impossible to tell without high-resolution Hα imaging of these systems.

4.1.1 Offset emission

In Hamer et al. (2012), we report on the nature of three objects (two from this sample) which show a significant component (>50 per cent) of their line emission significantly offset from the centre of the BCG. Fig. 7 (top) shows a histogram plot of the apparent visible offset between the BCG and the majority of the clusters line emission. It can be seen that almost all clusters show a small offset of less than 4 arcsec and most well below the seeing limit (∼1.5 arcsec). Only one object (Abell 1991) shows an offset of greater than this which makes it clearly stand out amongst our sample. In the middle panel of Fig. 7, we present the physical offset of the BCG from the majority of the line emission calculated at the redshift of the host cluster.

We draw three conclusions from this plot, the first is that the majority of the objects show a small physical offset as is expected. Secondly, we note that there are now two objects showing a significant offset, one at ∼10 kpc and one at ∼12.5 kpc. These objects are Abell 1991 and Abell 3444 which were studied in Hamer et al. (2012). Additionally, there is a cluster of objects with an offset of ∼6 kpc in Fig. 7. Studying the maps of these clusters, we note they are mostly plumes rather than separate offset emission. However, one of these objects is Abell 2566 which is offset and shows no line emission at the location of the continuum peak. In this respect, it is similar to the Ophiuchus cluster identified by Edwards et al. (2009).

Hamer et al. (2012) postulated that the apparent differences between Ophiuchus and Abell 1991/3444 may have been the effect of

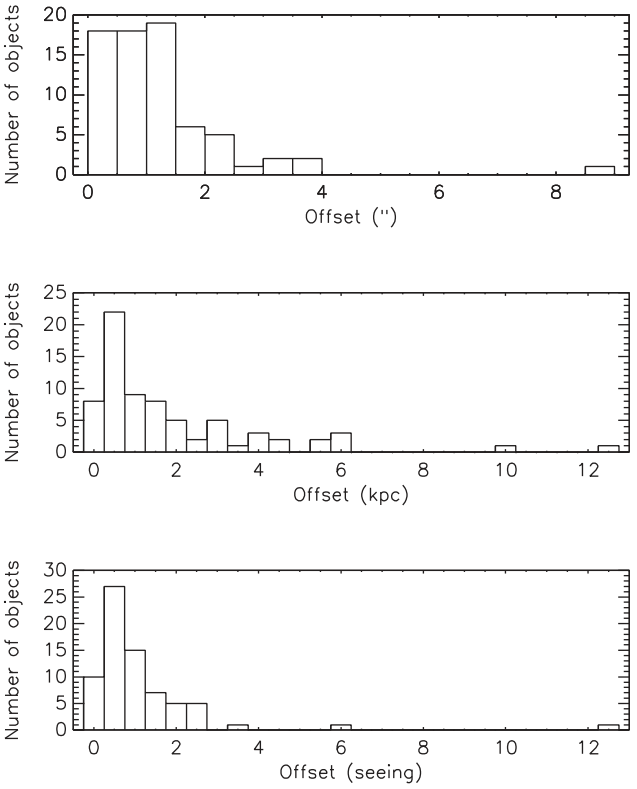

Figure 7. The top plot (a) shows the apparent offset between the continuum emission of the BCG and the centroid peak of the Hα emission for the full sample of objects. Almost all objects show small apparent offsets of less than 4 arcsec. Only one object shows a significant apparent offset, this is Abell 1991. The middle plot (b) shows the physical observed offset of the BCG and the majority of the line emission. Here we see a more spread out distribution of objects but with the majority still showing small offsets.The bottom plot (c) shows the offset as measured in terms of seeing units (offset in arcsec/mean seeing). We note that most objects are offset by less than 1 seeing unit confirming that there is no real offset in these objects. There are also two objects which show a very large offsets at 6 and 12.5 seeing units. These are Abell 3444 and Abell 1991, respectively, and clearly indicates that the offset in these objects is real.

viewing the offsets inclined at different angles to the plane of the sky. Ophiuchus had a physical offset of just 2.2 kpc but a dynamical offset of ∼600 km s^{-1} while Abell 1991/3444 have much larger physical offsets but dynamical offsets of the order of ∼100 km s^{-1}. Abell 2566 has an offset of 5.8 kpc putting it between the two extremes. Comparing the redshift of the Hα to that of the NaD from the BCG, we find a dynamical offset of 210 ± 21 km s^{-1}, which is consistent with this postulation.

Abell 2566 differs from the other offset objects which are studied in Hamer et al. (2012) in that it shows a possible close companion in the VIMOS field of view (Fig. 8). Comparing the NaD of the second galaxy to that of the BCG, we find a velocity difference of 279 ± 29 km s^{-1}, confirming it is a cluster member and not a foreground galaxy. This suggests the possibility that the two are strongly interacting. A FORS1 *R*-band acquisition image shows an extent of the continuum emission in the direction of the Hα similar to clumpy complex structures seen in other systems where the BCG and a companion are interacting. The offset objects previously studied showed no evidence of an interaction with another cluster member, so while Hamer et al. (2012) suggest an interaction as the likely cause of the offset, it was not possible to confirm it unambiguously.

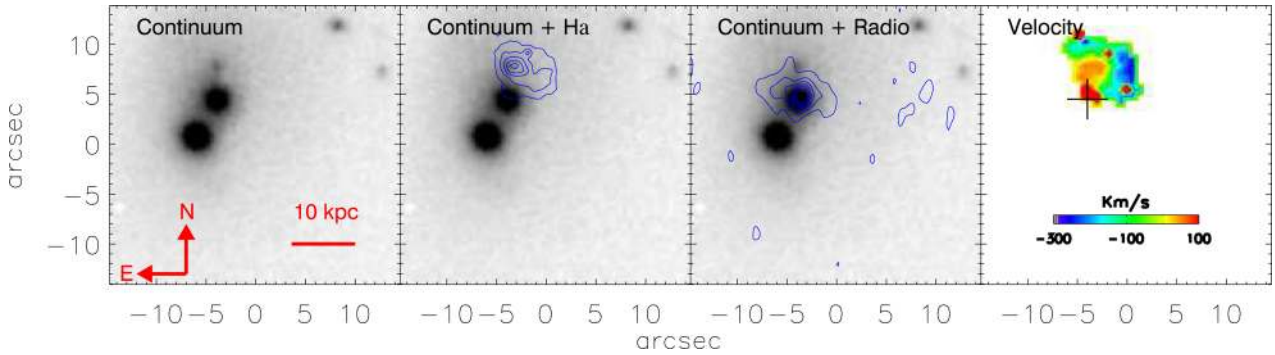

Figure 8. Left – FORS1 *R*-band image of Abell 2566, the BCG is the northern of the two objects. A region of low-surface brightness emission can be seen extending north from the BCG. Centre left – FORS1 *R*-band image of Abell 2566 with the H α emission contoured in blue. A clear offset between the BCG and the H α emission of ∼6 kpc can be seen. We note that the peak of the H α emission is coincident with the position of the extended low-surface brightness structure seen in the continuum image. Centre right – FORS1 *R*-band image of Abell 2566 with the radio map taken from Owen & Ledlow (1997) contoured in blue. Right – H α velocity field of Abell 2566 as shown in Appendix C. The cross on this image marks the centre of the BCG.

Unfortunately, Abell 2566 lacks high-resolution X-ray observations which are required to study the ICM in detail. So, while it may be tempting to speculate that the offset H α emission in this system is evidence of sloshing induced by an interaction, more detailed observations are required before this can be confirmed.

Fig. 9 (top panel) shows the physical offset against the cluster redshift for the whole sample. It can clearly be seen here that the offsets for the majority of the sample fall below the seeing limit of the VIMOS observations. Abell 1991 and Abell 3444 again clearly stand out from the sample, and we see the group of plumed objects (along with Abell 2566) at an offset of ∼6 kpc. The dot–dashed line in Fig. 9 marks the limit of the VIMOS field of view, assuming the BCG was at the centre of the pointing, objects with a separation placing them above this line would not be detected as the offset emission would fall outside the observed area of sky. The bottom panel of Fig. 9 shows a similar comparison between the centre of the clusters X-ray emission and the H α emission for objects with high-resolution X-ray observations. The X-ray centres are taken from the ACCEPT data base (Cavagnolo et al. 2009) with the exception of Abell 3444 for which we use the position defined in Hamer et al. (2012). Most of the objects have an offset close to the average seeing limit of VIMOS, suggesting that there is no significant offset seen. However, we note that three objects have an offset of more than 4 kpc that are significantly greater than the average seeing. One is Abell 133 which shows an offset 5 kpc (4.5 arcsec). We note that the continuum image of this object shows a bright source 4.5 arcsec to the north of the BCG which matches the position of the X-ray centre, suggesting that the true cluster centre may be obscured by a point source as was the case for Abell 3444 (Hamer et al. 2012). The other two objects are RXCJ 1539.5−8335 and RXCJ 2129.6+0005 which show large offsets of 8.4 kpc (6 arcsec) and 13.7 kpc (3.6 arcsec), respectively. RXCJ 1539.5−8335 may be erroneous as the VIMOS field of view only covers half of the BCG thus the position of the true peak of the H α emission is uncertain. RXCJ 2129.6+0005 is quite high redshift for the sample ($z = 0.234$) and we note that the seeing is above the average seeing limit suggesting the apparent offset may be a result of the seeing. However, the average seeing during the observations of this object was 1.8 arcsec, roughly half the observed offset so it cannot be explained due to seeing alone. Additionally, the position of the H α peak is well defined and no continuum source is present at the location of the X-ray centre, suggesting that this offset may be real. Further dedicated study of these three objects is required to confirm if these offsets are real, however, even if they

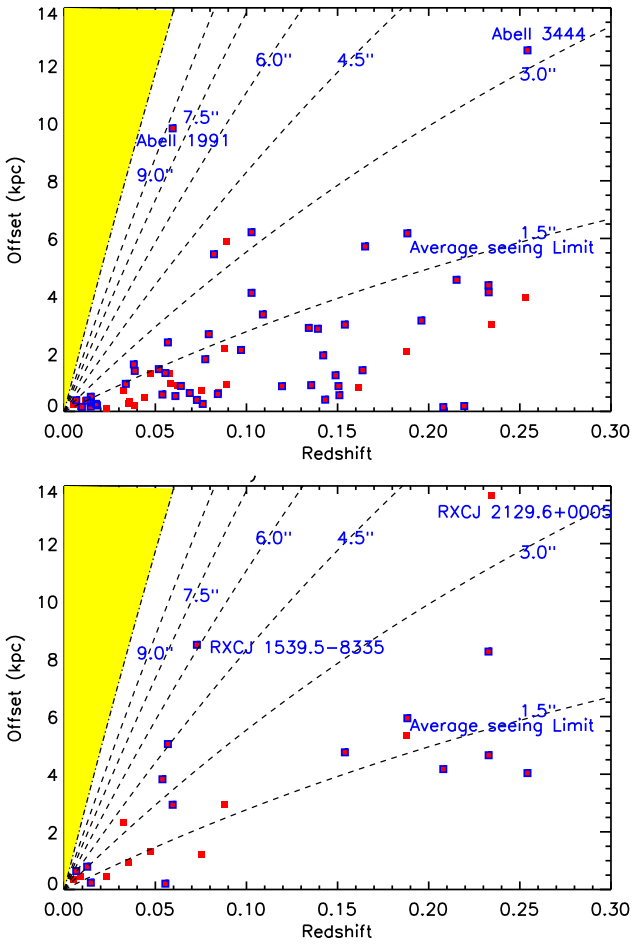

Figure 9. Top – observed physical offset between the BCG and the majority of the line emission at the cluster redshift. Bottom – observed physical offset between the centre of the clusters X-ray emission and the majority of the line emission at the clusters redshift. The dashed lines show constant visible offsets in 1.5 arcsec steps. We can see that the majority of objects fall well below the average seeing limit of 1.5 arcsec. The dot–dashed line shows the extent of the VIMOS field of view (∼12" assuming the BCG was positioned at the centre of the field of view) with the shaded region marking the extent beyond the field of view. Objects whose seeing during the VIMOS observations was less than 1.5 arcsec (the average seeing limit) have their points highlighted by a blue outline.

all are they account for just 12 per cent (3/24) of the objects studied. This would suggest that the optical line emission follows the X-ray peak in the majority of systems agreeing with the findings of Hamer et al. (2012).

Figs 7 and 9 highlight the difficulty in detecting offset emission with VIMOS observations. Due to the limited field of view, large offsets at low redshift would not be detected. Likewise, a smaller physical offset at the higher redshift end of our sample would have an apparent offset on the scale of the seeing (the offset in Abell 1991 would be <3 arcsec at the redshift of Abell 3444, for example) preventing its detection. We also note that objects with an offset along the line of sight would not be easily detected when considering only the structure of the ionized gas. The discovery of other offset objects does not significantly alter the statistics discovered in Hamer et al. (2012) with just 4 of the 73 objects in this sample showing offset emission; these objects account for less than 5 per cent of the line-emitting BCG population. If the sloshing of the ICM is responsible for these offsets, then it suggests that events capable of causing sloshing (such as a strong interaction) are rare or do not cause a major disruption of the cold gas reservoir.

4.2 Mean velocity structure

The velocity structure of the gas can also indicate if the gas is disturbed and may be a more reliable measure in systems where the lowest surface brightness gas may not have been detected. Maps of the mean line-of-sight velocity (from here on the mean velocity) structure of each object were produced from the parametrized fits so the velocity structure could be studied. The ionized gas in many of the cluster cores studied show a clear velocity gradient from negative to positive velocities relative to the systemic velocity. This velocity gradient is often seen to run across the bright peak of the line emission. Velocity profiles like these are often indicative of rotation but can also arise from uniformly entrained or out flowing material with an inclination to the plane of the sky. One caveat that must be considered here is the possibility that limited resolution in the higher redshift objects could smooth out variations in the velocity field and make the overall variation across the BCG appear as a much smoother gradient than is actually the case. To test this we take NGC 5044, a low-redshift ($z \sim 0.009$) object with a velocity field that shows a lot of variation, and degrade its resolution to that of a $z = 0.05$ object before refitting the cube and remaking the velocity maps. While this significantly reduces the small-scale variations in the velocity field seen in the higher resolution map, the overall velocity structure still does not show a smooth gradient like those seen in other objects, suggesting that limited resolution has only a small impact on our ability to distinguish between objects with a smooth velocity gradient and those without.

We define the peak-to-peak velocity to be the maximum velocity difference measured across the natural peak of the line emission. To calculate this, the velocity maps were first median-smoothed to eliminate any pixels with extreme velocities relative to their surrounding pixels. A ∼2 arcsec wide slit was then placed on the map centred on the peak of the line emission, in the case of objects with significantly offset emission, we use the peak of the continuum instead. This slit was then rotated through 180° in 6° increments, and at each position, a profile was extracted by interpolating along the slit and smoothing to 2 arcsec to reduce the noise. Fig. 10 shows an example profile from Hydra-A with the blueshift peak, redshift peak and peak-to-peak velocity indicated. The maximum velocity difference between the blueshift peak and the redshift peak (relative to the redshift at the centre of the H α emission) from these profiles

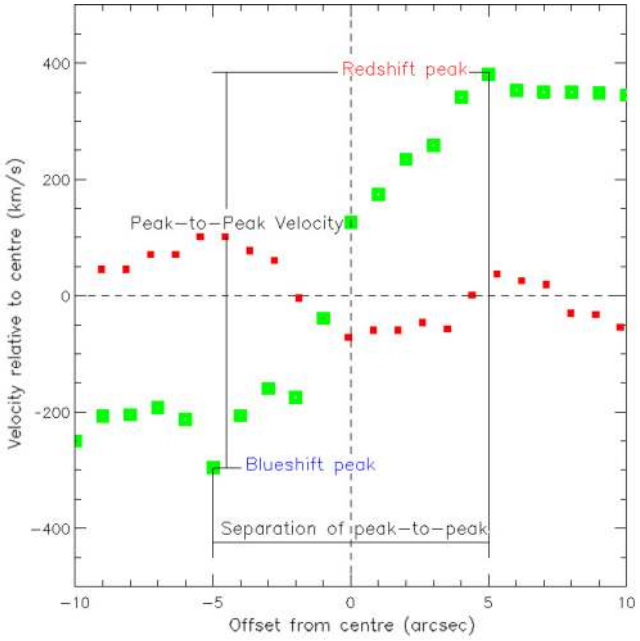

Figure 10. Two examples of a velocity profiles taken from Hydra-A (large green points) and NGC 5044 (small red points). These profiled were used to calculate the peak-to-peak velocity within each system. The contrast of these two objects shows how the peak-to-peak was clear in some objects (such as Hydra-A) while being much more difficult to constrain in others (such as NGC 5044). The blueshift peak and redshift peak are labelled and the peak-to-peak velocity and peak-to-peak separation are indicated for Hydra-A.

is then defined as the peak-to-peak velocity. This is the maximum velocity difference across the line emission as given in Table 2. One caveat to note is that the blueshift and redshift peaks were required to be on opposite sides of the centre. In some of the more disturbed velocity maps (NGC 5044, for example), the natural peaks did not occur on opposite sides of the centre, in such cases, the peaks were defined as the points which gave the maximum velocity difference across the centre of the H α emission.

Within the more extended and disturbed objects, the velocity maps show much more variation. However, under closer scrutiny, many of these objects do still often show smooth velocity gradients on smaller scales close to the centre of the system (defined by the location of the H α peak). The bright central region of these systems show a coherent velocity structure with a strong gradient across the centre of the system. Away from this central region, however, in the lower surface brightness-extended emission, the velocity field becomes much more chaotic. Abell 3581 and RXJ 0338+09 are two good examples of such objects, each show extended low-surface brightness emission with no coherence to the velocity structure. However, in the regions close (within ∼8 arcsec) to the peak of the emission, the velocity field shows much less variation. If it is the case that the extended emission is the result of some event which has disturbed the distribution of the cold gas, then this small-scale velocity structure may represent the overall velocity field of the object. Events, such as entrainment by radio jets or galaxy interactions which can disturb the cold gas, would initially affect the low-density gas at the edges of the distribution. The disturbance can impart a velocity on this gas which is not consistent with the overall velocity field of the system. The densest gas, however, is much more difficult to displace (Churazov et al. 2002) and, if it remains relatively undisturbed, should retain its previous velocity,

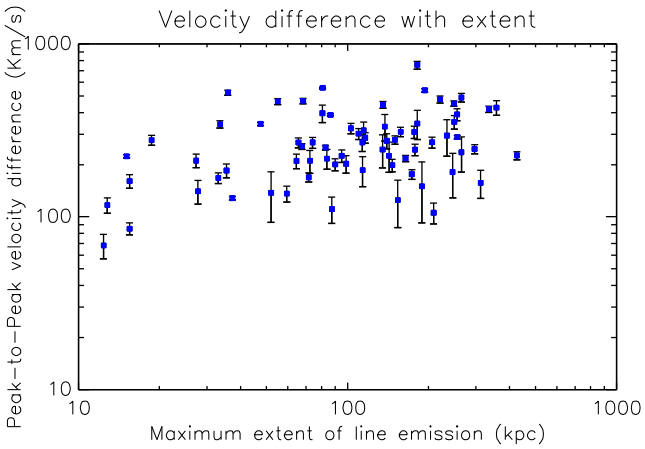

Figure 11. The peak-to-peak velocity difference against the measured extent of each object. It is clear that there is no trend with the exception that very compact objects show a reduced velocity difference. This suggests that the different peak-to-peak velocities seen between objects in the sample are not simply the effect of having gas sample a larger portion of the velocity field in some objects than in others.

which should be governed by the global velocity field within the cluster core.

If the velocity field of each object is roughly consistent, then any observed peak-to-peak velocity difference between them would simply be the effect of the gas sampling different regions of the velocity distribution. This would present itself as a clear trend between the extent of the line emission in a given object and the magnitude of the velocity difference observed.

In Fig. 11, we show the peak-to-peak velocity plotted against the maximum continuous extent of the line emission. A lower velocity difference is seen in very compact objects, however, as very compact objects are much more susceptible to blurring caused by the seeing, this trend may not be real. If the velocity difference is being measured over a region comparable to the seeing, it is possible that gas at each peak may be blended with some emission from the other peak resulting in a shifting of the best-fitting models closer together thus reducing the measured velocity difference. For objects with an extent of >2 kpc, the median-velocity difference of the objects remains constant at ∼250 km s^{-1} with a very large scatter. It is important to note, however, that any inclination of the velocity structure towards the plane of the sky will reduce the observed peak-to-peak velocity.

The average velocity gradient of each system can be calculated from the peak-to-peak velocity difference and the separation of the peak to peak (thus, $V_{\rm grad} = \Delta V/\Delta {\rm r}$). In Fig. 12, we plot the calculated values of velocity gradient for each object, the top two panels of this figure show the velocity gradient plotted against the two parameters used to calculate it (the peak-to-peak velocity and the separation of the velocity peaks). It can be seen from these plots that the measured velocity gradient of each object is well correlated with the separation with a smaller gradient in objects with a larger Δr. By contrast, the plot showing the velocity gradient against the velocity difference shows no obvious correlation. It is not unexpected that a correlation would be seen when plotting $\Delta V/\Delta {\rm r}$ against Δr. The simple expectation if ΔV and Δr are uncorrelated would be that $V_{\rm grad} \propto \Delta {\rm r}^{-1}$ and $V_{\rm grad} \propto \Delta V$. However, our best-fitting trend line has the equation $V_{\rm grad} = 160 \pm 1.2 \times \Delta {\rm r}^{-0.8\pm0.06}$, which is not consistent with this expectation. No significant trend is found in the plot of $V_{\rm grad}$ against ΔV; however, we note that higher values of the peak-to-peak velocity have (on average) higher velocity gradients. This is shown by the green diamonds which show the median velocity gradient within 50 km s^{-1} bins. It can be seen that at higher peak-to-peak velocities, the median velocity gradient is higher, as would be expected. The red dashed line shows the expected trend $V_{\rm grad} \propto \Delta V$ with the form $V_{\rm grad} = \Delta V$ / 10, the points of median velocity follow this trend (except at extreme velocities where few points are sampled) suggesting that the velocity gradient is proportional to the peak-to-peak velocity as is expected, albeit with considerable scatter.

In order to test the expected correlations, we replace the peak-to-peak velocity (ΔV) in our analysis with the total H α flux of an object. Since the H α flux comes from the full extent of each object, we expect it to have no correlation to the separation of the peak-to-peak velocity. We thus define $\mathrm{H}\,\alpha_{\rm grad} = {\rm F}_{\mathrm{H}\,\alpha}/\Delta {\rm r}$ and plot $\mathrm{H}\,\alpha_{\rm grad}$ against $\mathrm{F}_{\mathrm{H}\,\alpha}$ and Δr. We find that $\mathrm{H}\,\alpha_{\rm grad} = 62 \pm 1.5 \times \Delta {\rm r}^{-0.94\pm0.15}$ and $\mathrm{H}\,\alpha_{\rm grad} = 0.11 \pm 1.4 \times {\rm F}_{\mathrm{H}\,\alpha}^{0.97\pm0.09}$. Since the exponents of these equations are consistent with −1 and 1, respectively, the equations are consistent with our expectation that the total H α flux has no dependence of the separation of the peak-to-peak velocity. Thus, for two unrelated values, a and b, a/b ∝ a and a/b ∝ b^{-1}. Since the correlation of velocity gradient ($\Delta V/\Delta {\rm r}$) is proportional to $\Delta {\rm r}^{-0.8}$ not $\Delta {\rm r}^{-1}$ (Fig. 12) this suggests that ΔV already has some dependence on Δr that is a physical phenomenon, rather than a mathematical artefact. As such, the velocity fields have some structure as a function of radius.

One possible explanation is that the velocity field traces a rotation. On large scales, gas rotating under gravity should form a Keplerian disc about the centre of mass of the system. The rotation curves of discs are well understood and can be approximated to follow the curve of an arctan function (Courteau 1997) of the form

$$V({\rm r}) = V_0 + \frac{2}{\pi} V_{\rm c} \arctan({\rm R}), \qquad (2)$$

where $R = ({\rm r} - {\rm r}_0)/{\rm r}_{\rm t}$, V_0 is the velocity at the centre of rotation, r_0 is the spatial centre of the galaxy, $V_{\rm c}$ is the asymptotic velocity corrected for inclination ($V_{\rm c} = V_{\rm asym} \times \sin {\rm i}$) and $\mathrm{r}_{\rm t}$ is the radius at which the rotation curve transitions from rising to flat (where the rising part of the rotation curve has a gradient of 1). Thus, for a rotating disc, the velocity at a given distance from the centre of rotation can be assumed to be a function of that distance.

If the velocity field followed such a rotation then the expected peak-to-peak velocity (ΔV) would be 2 × the rotational velocity (V(r) from equation 2) and the separation (Δr) would be twice the maximum radius (r from equation 2). V_0 can be set to 0 as we are only interested in the velocity difference not the absolute velocity. We used equation (2) to produce 500 velocity profiles using randomly generated variables from within the parameter limits of our data ($V_{\rm asym}$ of 200–700 km s^{-1}, sin(i) of 0.0–1 and $\mathrm{r}_{\rm t}$ of 1–3 kpc). For each, we calculated the velocity gradient ($V_{\rm grad}$) and reproduced Fig. 12 for these models. We find a correlation between $V_{\rm grad}$ and the peak-to-peak velocity with the form $V_{\rm grad} = 130 \pm 1.1 \times \Delta {\rm r}^{-0.78\pm0.03}$ and no strong correlation of $V_{\rm grad}$ with ΔV which matches what is seen in the data. This suggests that the velocity structure in the majority of our objects may be consistent with disc-like rotation. However, we note that the velocity maps for some of our objects are very chaotic (e.g. NGC 5044) and clearly not dominated by rotation, thus a more detailed analysis is needed to identify rotation in these systems on a case by case basis. We will further explore the idea that the kinematics are related to a rotating disc in the next paper in this series but have already shown this to be true for one object (Hamer et al. 2014).

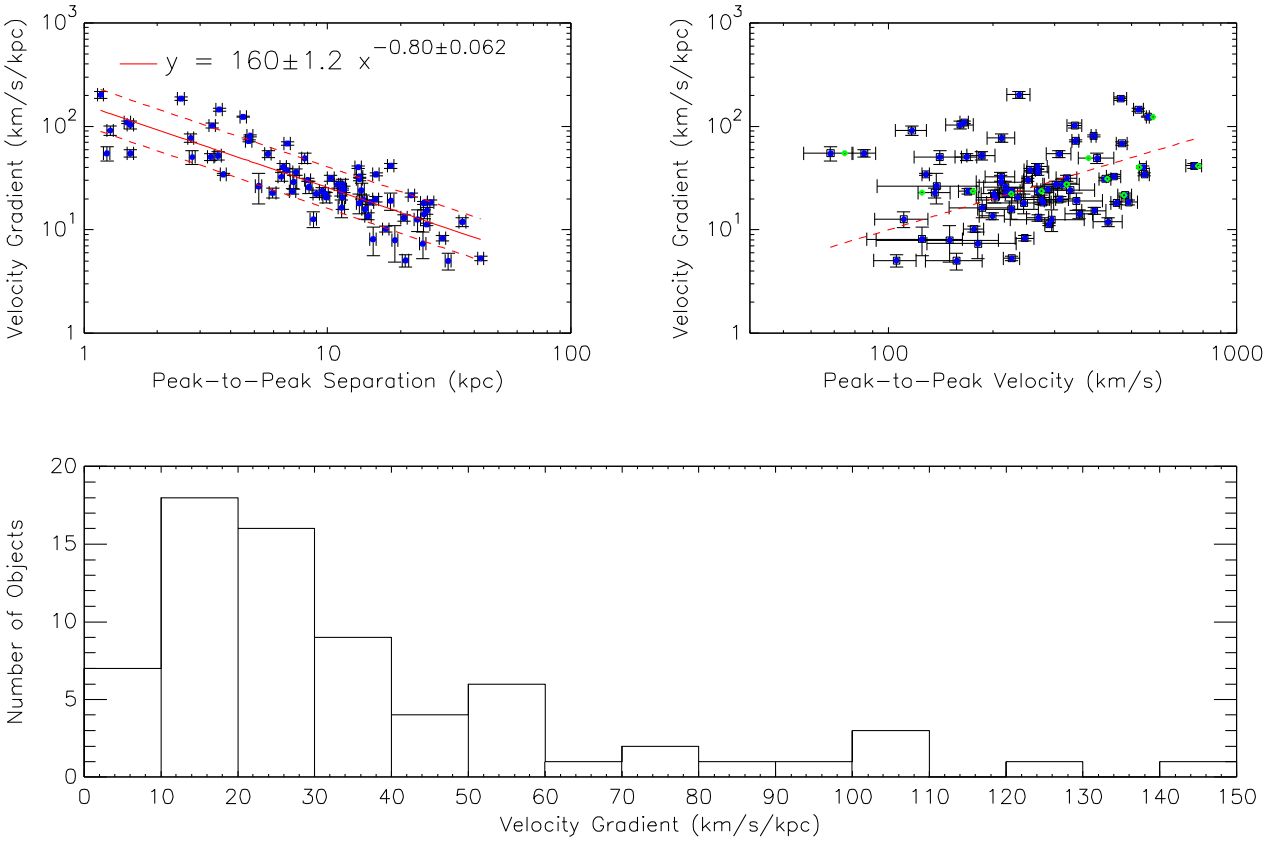

Figure 12. Top left – plot of the velocity gradient of every object in the VIMOS sample against the separation of the peak-to-peak velocity. A clear trend can be seen in this plot indicated by the red line and the equation of the best fit is given. Top right – in this plot, we compare the velocity gradient of our objects to the measured peak-to-peak velocity difference. No clear trend is seen, the dashed line shows a linear increase with velocity and the green diamonds show the moving average of the data. Bottom – this shows a histogram of the velocity gradients calculated for the objects in the VIMOS sample. A clear peak can be seen at ∼15 km s^{-1} kpc^{-1} with a steady decrease towards higher velocity gradients. This suggests that the velocity gradients seen in the sample are sufficiently small that their effect on the velocity dispersion should be negligible. The combined interpretation from the top two plots is that the velocity gradient responds to the separation of the peak to peak in a non-linear way while showing little correlation to the peak-to-peak velocity itself.

4.2.1 Velocity dispersion

The FWHM of an emission line is a measure of the velocity dispersion of the gas from which it was emitted. In observations with ordered motions (such as a difference in the mean velocity), the velocity dispersion is a measure of the random motions of the particles which make up the gas. There is of course some care required in this interpretation as it requires the assumption that the variation of any ordered velocity field, within the region the spectrum is extracted from, is negligible compared to the random velocities within that same region. Fig. 12 also shows a histogram of the mean velocity gradients for each object in the sample. From this, it can be seen that the velocity gradient for most objects is quite low with the distribution peaking at ∼15 km s^{-1} kpc^{-1}. This suggests that the velocity gradients seen in the sample are sufficiently small such that their effect on the measured linewidths should be negligible.

We give the average linewidth measured within the central ∼2 arcsec × 2 arcsec region of the system in Table 2. We note that the gradient of the clusters velocity field should be highest in the centre where the mass concentration naturally peaks and it is within this region that the velocity dispersion is most likely to be broadened by the velocity gradient. The region used to extract the FWHM is comparable to the mean seeing (∼1.5 arcsec) and is thus the scale on which we would expect the mean velocities to be blended.

In Fig. 13, we show the average velocity dispersion within the central 2 arcsec × 2 arcsec of each objects plotted against the peak to peak of the mean velocity field. If we ignore the points with a peak-to-peak velocity below 100 km s^{-1} (i.e. below the spectral resolution of the `HR_Orange` and `HR_Red` VIMOS gratings), this plot would suggest that there is no obvious correlation between the average central velocity dispersion and the peak-to-peak velocity difference for our sample. We performed a Spearmans test to confirm this lack of correlation and find that $\rho = -0.016$ with a p-value of 0.9 confirming the lack of correlation. This lack of correlation confirms the assumption that the velocity dispersion measured is real and not an effect of blending gas clouds with different mean velocities. Higher spectral and spatial resolution data would be required to study the broad-line regions in more detail.

The maps of most objects show an FWHM profile which peaks towards the centre of the system, where the flux map peaks, and falls away as the surface brightness of the line emission does. This linewidth profile is exactly what is expected as in the central regions there should be a higher projected mass density. Within most objects, the extended low-surface brightness gas has a consistently low FWHM of the order of ∼100–200 km s^{-1}. Interestingly some objects show additional peaks in the linewidth away from the centre, suggesting the gas is more kinematically disturbed in these regions. Indeed the fact that most of these offset FWHM peaks appear in

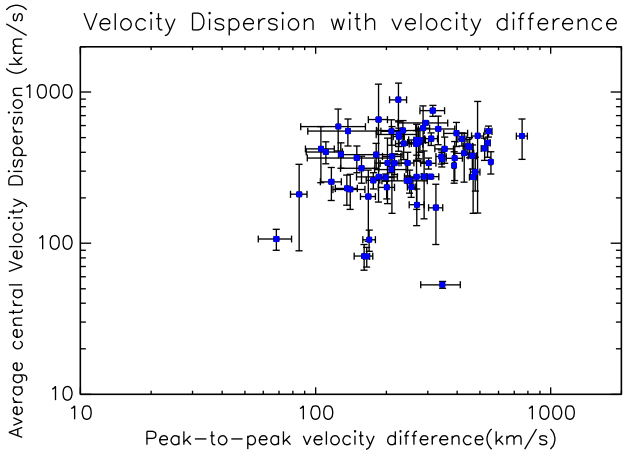

Figure 13. Plot of the central velocity dispersion (FWHM) against the peak-to-peak velocity difference of each object. If the outliers with very low-velocity dispersion (<100 km s^{-1}) and/or low-velocity difference (<100 km s^{-1}) are ignored, then there is no obvious trend suggesting the velocity dispersion is unrelated to the velocity across the object. This confirms the assumption that the velocity dispersion measured is real and not an effect of blending gas clouds with different mean velocities.

systems with spatially disturbed morphologies (Abell 3574, RXJ 0338+09) would seem to support this assumption.

4.3 Statistics of the sample

In Fig. 14, we plot the Hα luminosity against the extent for each object. As would be expected, we see a clear trend in this plot with the more luminous objects being more extended due to the increased surface brightness. The points on the plots in Fig. 14 are colour coded, in the top plot, by the peak-to-peak velocity, and in the middle, by the [N II]/Hα ratio (see Section 5 for a discussion of the line ratio analysis). The top plot of Fig. 14 shows no general trend of the velocity, as might be expected from the lack of a trend in Fig. 11. We do note however that the lowest luminosity (<10^{40} erg s^{-1}), most compact objects (extent <3 kpc) have low peak-to-peak velocities with all but two falling into the lowest velocity bin. The middle plot of Fig. 14 shows how the [N II]/Hα ratio varies with the extent and luminosity. Again, we note that the objects to the lower left (compact and low luminosity) have quite consistent [N II]/Hα ratios with all but two falling into the highest bin. So collectively from Fig. 14, we can identify a collection of objects with low extent and luminosity, little velocity structure and high-ionization states. We would therefore suggest that the majority of the objects in Fig. 14 below an Hα luminosity of $\sim 4 \times 10^{39}$ erg s^{-1} with an extent less than 4 kpc are most likely to be low-ionization nuclear emission-line regions (LINERs). The bottom plot of Fig. 14 colour codes the points by redshift bin. The higher redshift sources are typically brighter and more extended as would be expected for a flux-limited sample.

In Fig. 15, we compare each objects Hα luminosity with its peak-to-peak velocity. There is no trend immediately apparent from this plot as might be expected given the trend between luminosity and extent, and apparent lack of trend between velocity and extent. When considering an observed velocity structure, it is always important to consider the effects of inclination which can reduce the observed peak-to-peak velocity regardless of the origin of the velocity structure. The most likely inclination to view a velocity structure along, given a heterogeneous population and unbiased sample (a fair

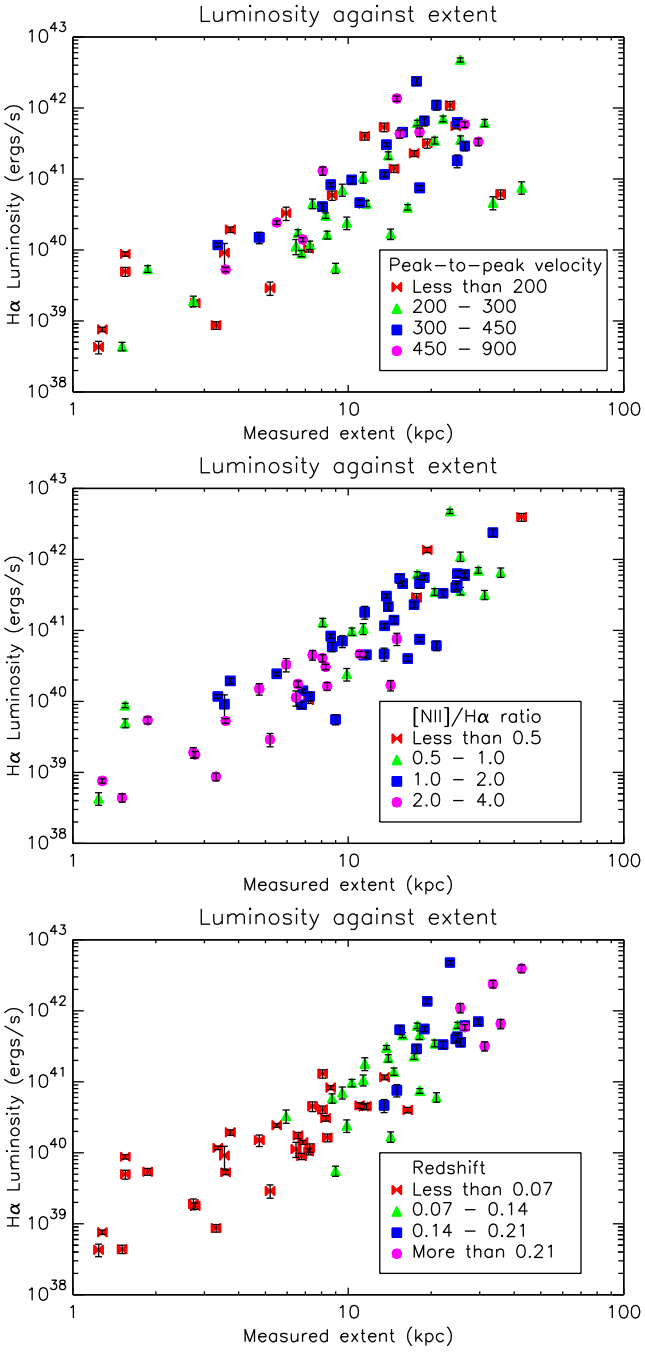

Figure 14. The Hα luminosity plotted against the extent of the line-emitting region. A clear trend can be seen between the luminosity and extent as would be expected. Top – the points are colour coded into bins of peak-to-peak velocity. The velocity shows no clear trend on this plot, however, we do note that the most compact (with an extent of less than 3 kpc) and least luminous objects have low velocities with all but two falling into the lowest velocity bin. Middle – the points are colour coded into bins of overall [N II]/Hα ratio. The trend of [N II]/Hα ratio with extent can be seen in this plot. Again, we see that the low-luminosity compact objects typically have high [N II]/Hα ratios. Bottom – the points are colour coded into redshift bins. The higher redshift sources typically show higher luminosities as would be expected for a flux-limited sample.

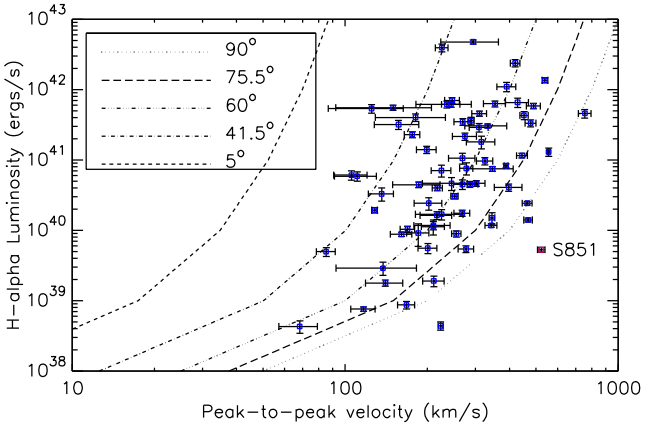

Figure 15. The H α luminosity plotted against the peak-to-peak velocity. It is apparent from this plot that the mean velocity of the sample is dependent on the luminosity. This may be an effect of the more H α luminous systems being more massive or that we can detect H α sampling more of the velocity field in the more luminous systems. The lines on this plot show what the velocity would be at a given inclination if we assumed this trend was true, took the median velocity in each luminosity bin and assumed this came from an object inclined at 60° to the plane of the sky (the most likely inclination of an unbiased sample). In such a case, the velocity of only one object in the sample, S851, cannot be explained by an inclination effect alone.

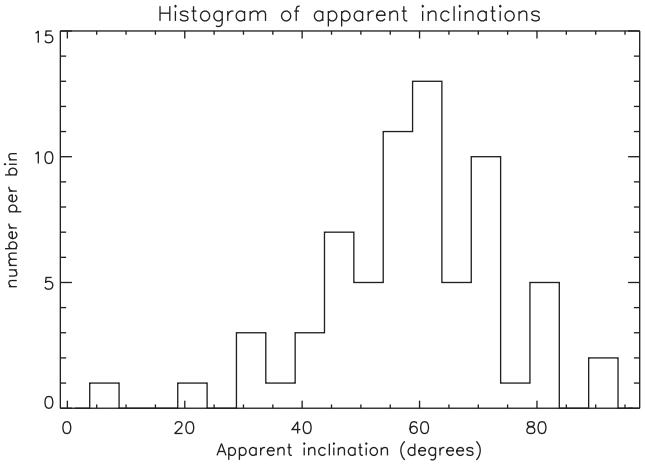

Figure 16. Here, we show the apparent inclination of the objects in the sample if it is assumed that the variation in their velocity at a given luminosity is a function only of inclination. The apparent inclination of the velocity is relative to the plane of the sky such that a velocity in the plane of the sky would have an inclination of 0°. There is a peak at ∼60° around which the apparent inclinations are distributed likely caused by noise obscuring face-on systems and degeneracy between the effect of inclination and natural variations of the peak-to-peak velocity.

assumption for our objects given the minimal selection criteria), is 60° to the plane of the sky. If we assume that the average velocity for each luminosity bin is from an object at this inclination, then we can show how this trend would be affected by the inclination. We selected a number of inclinations which would split the velocity range approximately into quarters, these inclinations are plotted as a series of lines in Fig. 15. We can see that the same trend shifted to 90° encloses all of the objects in the sample bar one, S851. If we ignore the single outlier, then it is possible to account for the different velocities seen in objects with similar luminosities as purely an effect of inclination.

If we assume this distribution in velocities to be a result of the inclination of the system, then we can calculate the apparent inclination angle of each system using its luminosity and peak-to-peak velocity. In Fig. 16, we show a histogram of this apparent inclination for the systems in the sample. This plot shows that the velocity structure of the systems are distributed about an apparent inclination of 60° to the plane of the sky. There are very few objects with an apparent inclination around 0° and few with an inclination of greater than 80°. This distribution is consistent with what is typically seen when calculating the inclination of galaxies from their axial ratios. It is important to note, however, that using such a method has degeneracy with the thickness and ellipticity of the galaxy (Tempel, Stoica & Saar 2013). Thus, edge-on and face-on disc galaxies have their inclination incorrectly calculated resulting in a distribution similar to that in Fig. 16. However, the method used to determine the inclination in Fig. 16 is not subject to these same degeneracies and thus the distribution should be constant with $\sin(\theta)$. The lack of face-on systems can be explained by the fact that the measurable true peak-to-peak velocity difference would be very small. In such a situation, the velocity field will be dominated by noise, obscuring face-on systems. We also note that some scatter in velocity at a given luminosity is expected, especially given the size of the luminosity bins used (an order of magnitude). So the highest velocity systems in a given bin may skew the mean, thus making naturally lower velocity systems appear more inclined resulting in an underabundance of edge-on systems.

4.4 Comparison to the stellar kinematics

The sodium D stellar absorption features ($NaD_{\lambda 5895.9}$ and $NaD_{\lambda 5889.9}$) allows for the extraction of stellar kinematics but it requires the continuum emission to be bright in order for the absorption feature to be visible in the spectrum. It is also intrinsically a broad feature which makes contamination by sky lines a serious problem. We performed the fitting using Voigt absorption profiles following the same procedure used to fit the Gaussian emission line profiles. From the sample, only 12 objects had spectra in which the NaD absorption was clear enough to be fitted at the 7σ significance level (so as to match the emission lines).

While these objects all show a strong continuum and strong NaD absorption, they are otherwise quite dissimilar in their X-ray and optical properties. They have X-ray luminosities in the range of 0.1 – 42.10 $\times$ 10^{43} erg s^{-1} and H α luminosities in the range of 0.087 – 46 $\times$ 10^{40} erg s^{-1} which is representative of most of the objects in our sample. We note that none of the most luminous systems (either in X-ray or H α) appear in this sub-sample. However, such objects make up only a small fraction of our sample. The 12 objects show no common features in their other optical properties (velocity, extent, FWHM, [N II]/H α ratio and morphology) and were observed in a wide range of seeing conditions (0.63 – 2.39 arcsec), suggesting they are representative of the sample. We do note that the objects are all typically low-redshift sources (11 out of 12 have $z < 0.06$) but this is the result of the requirement for bright continua to detect the NaD absorption feature.

Recent studies have separated the NaD absorption in star-forming galaxies into two components (one from the stars and one from the interstellar medium) by fitting stellar population models to isolate the stellar component (Heckman et al. 2000; Jiménez-Vicente et al. 2007). This may be possible for the brighter objects in our sample through binning to increase the S/N. However, we expect the stellar component to be dominant in our systems as NaD is strong in the

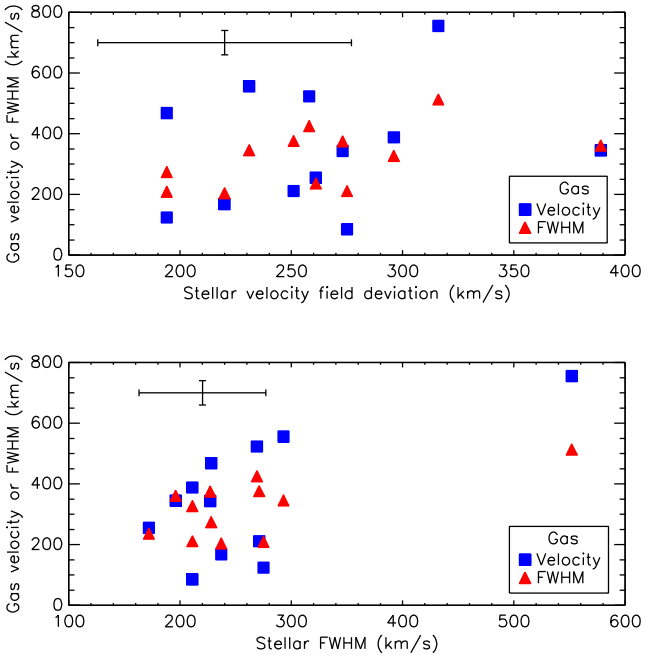

Figure 17. Top – ionized gas peak-to-peak velocity and FWHM compared to the standard deviation of the stellar velocity field. Bottom – ionized gas peak-to-peak velocity and FWHM compared to the overall FWHM of the stellar absorption. No trend can be seen in either of these plots suggesting that the ionized gas kinematics are decoupled from the stellar component of the BCG. Representative error bars are shown in the top left of each plot.

spectrum of cool stars (Jacoby, Hunter & Christian 1984) common in BCGs and is one of the strongest optical stellar absorption lines in the spectra of early-type galaxies (Heckman 1980; Bica et al. 1991). As such, given the focus of this paper is on the ionized gas emission, we assume that all the NaD absorption is stellar in origin.

We produce maps from the fits to the NaD absorption feature for these 12 objects and compare them to the line emission maps (see Appendix D). Determining the velocity dispersion of the NaD absorption from these line fits is not a trivial calculation and the fits themselves constantly overestimated the FWHM. To account for this, we used the fitting method to fit the total spectrum of each object and compared the FWHM derived by this method with the FWHM derived by fitting stellar templates to the same spectrum using penalized pixel-fitting (Cappellari & Emsellem 2004, which could not be used on individual pixels due to insufficient S/N). In this way, we calculated a normalization factor for the FWHM in each object and applied this to the velocity dispersion maps.

One thing that is immediately apparent from studying the NaD absorption maps is that the stellar component of the BCGs shows no evidence of an ordered velocity structure. Indeed, the mean velocity field appears to be completely random which is expected for a massive elliptical galaxy such as a BCG. This is in stark contrast to the ordered velocity maps produced from the Hα emitting gas. We also note that although the linewidth maps do generally show a peak towards the centre of the object they are overall substantially more uniform than their counterparts from the line emission. This implies that the stellar component of the BCGs has a velocity field which is dominated primarily by random motion suggesting that the movement of the stars and gas in the galaxy are decoupled. In Fig. 17, we compare the kinematics of the gas to those of the stars. No trends can be seen for any of the comparisons in this figure, however, we note the large errors on the parameters from the stellar fits make this ambiguous.

To test this, we performed a Monte Carlo procedure to reproduce the plots with parameters sampled from within the Gaussian errors shown. We produced 10 000 of each of the four comparisons: stellar velocity against gas velocity, stellar velocity against gas FWHM, stellar FWHM against gas velocity and stellar FWHM against gas FWHM. For each, we performed a Spearman correlation test and found no correlation in 90.0 per cent, 87.6 per cent, 88.9 per cent and 89.2 per cent of the realisations respectively. This lack of correlation confirms that the kinematics of the ionized gas are decoupled from those of the BCGs stellar component. Hydra-A is a clear example of this, it is one of the most ordered velocity fields in our sample and also has one of the largest peak-to-peak velocities. Moreover, it is known that the gas forms a rotating disc (Simkin 1979; Hamer et al. 2014), despite this, however, the stellar motions appear to remain random, producing a velocity field with no obvious order.

In Section 4.1.1, we identify Abell 1991 as an object with offset line emission. The extent of this offset can be seen in the maps comparing the stellar absorption to the ionized gas emission which can be found in Appendix D. While both have a peak in roughly the same position, the line emission map shows little emission around this point with most of it located ∼10 arcsec to the north where it shows a second peak. By contrast the majority of the NaD absorption is centred almost uniformly around the southern peak of the line emission with possibly a slight extent to the south. The comparison of the line emission maps with the stellar absorption maps clearly highlights this offset.

The line emission map of RXJ0338+09 shows a very disturbed morphology suggesting that some major event is disrupting the line-emitting gas within this system. Interestingly, the stellar absorption map shows a secondary peak of absorption at ∼7 arcsec (∼4.7 kpc) to the north-west of the BCG. This suggests the presence of a second galaxy very close in projection to the BCG. Consulting the stellar velocity map, we find that this galaxy also has a velocity which is close to that of the BCG, redshifted by just a few hundred km s^{-1} and matching the velocity of the line emission at this point. It is tempting to interpret these findings as evidence of an interaction which is disrupting the cold gas in the cluster core. However, we note that the companion galaxy has a bright X-ray point source (Sarazin, O'Connell & McNamara 1992) suggesting AGN activity, so it is possible that the Hα emission seen at the redshift of the companion is associated with its nucleus and superimposed on that of the cluster core. Additionally, the ICM shows evidence of cavities from multiple AGN outbursts (Sanders, Fabian & Taylor 2009) which may be responsible for disrupting the gas on large scales. Finally, the ro-vibrationally excited molecular gas appears to form a rotating structure close to the BCG (Wilman et al. 2011). Thus, to fully characterize the nature of the 'interaction' in this system requires a dedicated study of the complex processes at work using high-sensitivity multiwavelength observations and is beyond the scope of this paper.

5 THE PHYSICAL PROPERTIES OF THE GAS

In order to investigate the spectral differences between the objects, we now present spectra extracted from two regions for each object in our sample. We initially extracted spectra from the full region of line emission for each object. We defined this extent as being the region where the Hα flux exceeded the noise by a factor of 7. To determine this, we first collapsed the cube (see Section 2 for a description of this procedure) over the region of the spectra

containing the Hα emission. Additionally, we collapsed the cube over two other regions of equal spectral length which contained no emission lines or sky lines to produce two continuum images. A continuum-subtracted Hα map was then produced by subtracting the first of these continuum maps from the Hα map. The first continuum image was also subtracted from the second continuum image to produce a map from which the noise could be determined.

A mask was then produced to exclude spatial pixels where the Hα emission did not exceed a S/N of 7. The flux in the remaining pixels was then summed for each channel to produce a spectra of the full Hα emitting region. A second spectra for each object was extracted from the nuclear region of the BCG, defined as a 3 × 3 pixels ($\sim$2 × 2 arcsec^2) region (roughly the extent of the mean seeing) centred on the peak of the continuum emission. All spectra were sky and continuum subtracted, and have been filtered to eliminate contamination by cosmic rays. The two spectra from each object can be found in Appendix E and the line fluxes and ratios are given in Appendix F.

Our IFU observations of these clusters allow us to study the physical properties of the gas within the ionized nebulae using the ratios of the various optical emission lines visible in these spectra. Many of the lines commonly used in such analysis (Hα, [N II], [O I] and [S II]) are covered by our observations for all objects and are detected in most (see Table 1). Importantly as our observations are resolved, they allow us to determine how the properties of the gas vary throughout the nebula. However, some care must be taken with this analysis, especially as we lack the [O III]/Hβ ratio (commonly used in conjunction with the other line ratios for this kind of analysis), as there are many factors which can all affect the observed line ratios.

5.1 Metallicity

The line ratios are subject to change due to variations in the metallicity of the gas with the [N II]/Hα being the most strongly affected, $\log_{10}$([N II]/Hα) varies linearly with metallicity until it saturates at $\log_{10}$([N II]/Hα) ~ -0.5. For cool core clusters, metallicity profiles of the ICM are consistent between objects (Böhringer & Werner 2009), falling from close to solar metallicity in the BCG to $\sim$1/3 solar metallicity (Loewenstein 2004) in the ICM (beyond $\sim$0.25 r_{200}). We thus expect that the metallicity of the gas is approximately the same in all of the objects and, as our observations only cover at most a few tens of kpc, that any change in metallicity within a given object will be small. Thus, the metallicity should have a negligible effect on the variation of line ratios both between objects and within a single object when compared to other effects.

As all objects in our sample have Hα and [N II] emission, we can test this assumption by using the *N*2 index to estimate the metallicity of the gas in each of our objects as measured by the oxygen abundance (O/H). We use equation 1 from Pettini & Pagel (2004) to estimate the range of oxygen abundances in our sources from the [N II]/Hα ratio. From Table 2, we see that the maximum and minimum mean [N II]/Hα ratios in our sample are 3.7 and 0.54, respectively, which corresponds to oxygen abundances (12 + $\log_{10}$(O/H)) of 9.22 and 8.75. Pettini & Pagel (2004) find that 95 per cent of their measured oxygen abundances lie within ±0.41 of the value derived for a given [N II]/Hα ratio. Our two extremes fall well within these limits suggesting that the metallicities within all our objects are consistent. For objects where we also have the [O III] and Hβ lines, we can further test this consistency by using the *O*3*N*2 index as an additional measure of the oxygen abundance. Using equation (3) from Pettini & Pagel (2004), we estimate the oxygen abundances for the seven sources for which we could obtain the [O III]/Hβ ratios. We find oxygen abundances (12 + $\log_{10}$(O/H)) of 8.67–9.16 which are consistent with the values derived from the [N II]/Hα ratios. As such, we assume that the metallicity is the same in all objects and has no effect on the measured line ratios.

5.2 Electron density

The density of the gas can also have an effect on the line ratios measured for a given excitation mechanism. Importantly models of star formation excitation often used to distinguish between star-forming galaxies and those excited by more energetic phenomena typically assume electron densities of a few hundred or less (for example, Dopita et al. 2000; Kewley et al. 2001). The strengths of several lines in our observations are sensitive to the electron density but in particular, the [S II] doublet line fluxes, available for all but a few objects in our sample, are sensitive to the effects of collisional de-excitation. Since both lines have very similar excitation energies, their relative excitation rates are almost insensitive to variations in electron temperature. As such, the effect of temperature is negligible and the relative excitation rates of the two lines depend only on the ratio of their collision strengths and thus the ratio of intensities depends only on the density of the gas (Osterbrock 1989). This analysis is only sensitive to densities over $\sim$1 to 2 orders of magnitude between 100 and 10^4 cm^{-3}, fortunately, this is consistent with the densities assumed in models of star formation excitation and we expect the electron density in the cores of clusters to be towards the lower end of this density range. In Fig. 18, we plot the

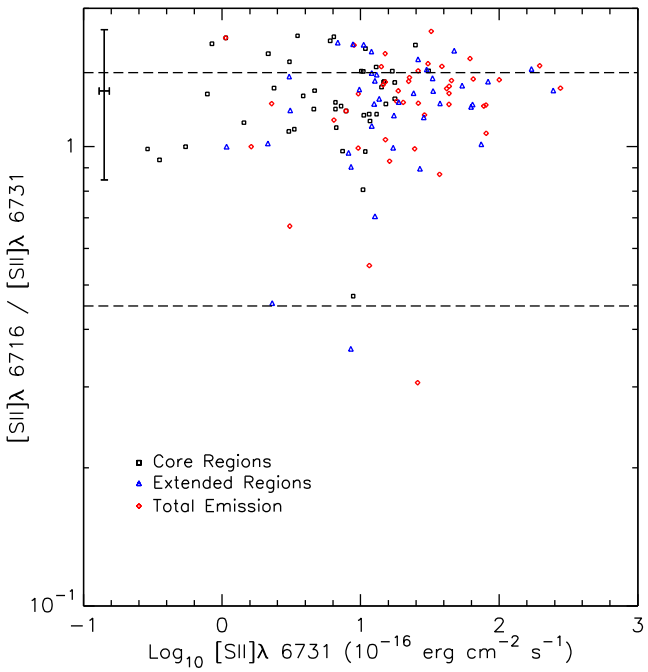

Figure 18. A comparison of the [S II]$_{\lambda6716}$/[S II]$_{\lambda6731}$ ratio and [S II]$_{\lambda6731}$ flux for all objects in the sample which had detections of both lines. The points show the core regions (black squares), extended regions (blue triangles) and total emission (red diamonds) for each object. The dashed lines indicate upper and lower bounds where the [S II]$_{\lambda6716}$/[S II]$_{\lambda6731}$ ratio is sensitive to changes in electron density. The upper boundary is set to a value of 1.45 corresponding to a density of $\sim$100 cm^{-3} and the lower boundary to a value of 0.45 corresponding to a density of $\sim 10^4$ cm^{-3}. Most of the points fall towards the upper boundary suggesting densities commonly in the region of a few 100 cm^{-3}.

[S II]$_{\lambda6716}$/[S II]$_{\lambda6731}$ ratio against the [S II]$_{\lambda6731}$ flux for all objects in the sample. The dashed horizontal lines on this plot contain the region that is sensitive to density changes. The majority of the points are found towards the upper boundary of this region suggesting that most objects in our sample have electron densities of the order of a few 100 cm^{-3}. We also note, however, that a small number of points (just four) fall within the region below a value of ∼0.7 suggesting these objects have densities in excess of 10^3 cm^{-3}.

The fact that some points fall outside of the region sensitive to density must also be considered. Some of these can be accounted for by the fact that in some cases some or all of the [S II]$_{\lambda6716}$ line fell into an atmospheric absorption feature and was lost. An example is Abell 795 which has a ratio in its core of ∼0.2 despite relatively strong lines being present as the [S II]$_{\lambda6716}$ line is redshifted into the atmospheric *A* band. A similar situation also affects some of the objects which have a ratio above 1.45. In this case, the [S II]$_{\lambda6731}$ line falls into the absorption feature causing the [S II]$_{\lambda6716}$ to appear unusually strong. Some of these points can also be attributed to objects whose redshifts put the [S II] lines right at the edge of the spectral coverage of our observations. In some cases, this resulted in some of the [S II]$_{\lambda6731}$ line falling off the edge of the spectrum in part or all of the field of view. Objects with such obvious factors causing errors in the [S II] flux measurements have been removed from the analysis in Fig. 18. There remain, however, many objects with ratios falling above a threshold of 1.45 and still two that fall below a ratio of 0.45. We note, however, that the errors on the ratio are considerable, in Fig. 18, we show representative errors positioned at the median ratio of [S II]$_{\lambda6716}$/[S II]$_{\lambda6731}$. We note that the upper error limit encompasses most of the points above a ratio of 1.45, as the majority of our objects tend to have high [S II]$_{\lambda6716}$/[S II]$_{\lambda6731}$ ratios (above ∼0.8), these errors can explain the large number of points falling above our expected upper limit. Indeed, the majority of ratios fall within these errors, suggesting that they are consistent with the median ratio of 1.32 which corresponds to densities of the order of 100–200 cm^{-3}. As such, the measured gas densities are consistent with those used in models of star formation so we can use the expected line ratios from such models to determine if star formation plays a major role in the excitation of the ionized gas in cluster cores.

5.3 Excitation state

The [N II] to Hα ratio is also a good measure of the excitation state of the gas and, in particular, is a good indicator of even small contributions to the excitation from an AGN thanks to its sensitivity to metallicity. The $\log_{10}$([N II]/Hα) ratio saturates at high metallicity peaking at ∼−0.5 (Denicoló, Terlevich & Terlevich 2002; Kewley & Dopita 2002; Pettini & Pagel 2004; Kewley et al. 2006), as such, [N II]/Hα ratios of above ∼0.6 are a strong indicator of an AGN (or other non-star formation) contribution to the excitation. Table 2 lists the mean [N II]/Hα ratio for all objects in our sample as calculated from the fits to each pixel. The ratio varies substantially between objects suggesting that some objects are substantially more highly ionized than others. As noted earlier, some of the objects showed Hα emission which was absorbed, this will have the effect of artificially rising the [N II]/Hα ratio calculated from fits to the total spectrum. We clearly indicate which objects show Hα absorption in Table 1. For these objects, the [N II]/Hα ratio calculated and presented in Table 2 can at best be considered an upper limit.

For the majority of objects, the [N II]/Hα ratio can be seen to vary within the maps presented in Fig. 4 suggesting that the ionization state is not constant throughout the objects. This is not surprising as sources of ionization (AGN, star formation, shocks, etc.) are often seen to be localized to specific parts of a galaxy (AGN are localized to the centre of the galaxy, star formation is often seen to be clumpy rather than uniformly distributed; O'Dea et al. 2010). The maps also indicate the regions of objects which have substantial Hα absorption as the [N II]/Hα ratios are extremely high appearing white on the maps.

While the maps show a lot of variation in the ionization state within different regions of each object, the line ratios do not show any obvious structures. Studying the overall ionization state allows for a direct comparison between objects and with other global parameters. The ionizing radiation within galaxies is believed to come from two primary sources, AGN and star formation (Baldwin, Phillips & Terlevich 1981). AGN typically produce a harder radiation field which results in a higher ionization state while star formation has a softer radiation field. Thus, one would expect gas ionized by AGN to have a high [N II]/Hα ratio while that ionized by star formation should have a lower value. However, this distinction is more complicated for gas in BCGs where both AGN and star formation are likely to be occurring. Shocks, produced from either internal (e.g. AGN outbursts) or external (e.g. galaxy interactions) sources, can also produce optical line emission. Generally, faster shocks produce higher line ratios (though there is also a dependence on metallicity, gas density and magnetic fields, Allen et al. 2008) comparable to those produced by AGN. However, if such fast shocks were present, they should be visible in Fig. 4 as broad regions in the FWHM panel. Post-asymptotic giant brach stars have been shown to be a possible source for LINER-like emission (Singh et al. 2013) which can produce line ratios inconsistent with star formation models. Other possible sources of the ionization include photoionization by emission from the hot gas in the ICM or collisional heating (Ferland et al. 2009; Fabian et al. 2011) which can also produce high [N II]/Hα ratios.

The majority of the extracted spectra show little variation in appearance between the central region and the total emission suggesting that an AGN is not significantly affecting the distribution of ionizing radiation in most objects. However, some objects do show a variation in the [N II] to Hα line ratio, which might suggest the influence of an AGN. Indeed, for some objects, the [N II] to Hα ratio is sufficiently high (above [N II]/Hα ∼ 0.6) to rule out star formation as the dominant component of the ionization. One striking observation from the spectra is the fact that some objects, which show strong lines in their total spectrum, have little or no emission present in their central regions. These are objects in which the peak of the line-emitting gas is offset from the BCG which results in weak or absent lines at the peak of the continuum emission. Such objects are discussed in Section 4.1.1 and studied in detail in Hamer et al. (2012) and while interesting, make up only a small fraction of BCGs (just four of the objects in our sample are offset in this way) and are thus not representative of the population.

In Fig. 19, we show the global measure of the [N II]/Hα ratio of each system as a function of the extent of its line-emitting region. With the exception of a few outliers this plot shows a trend with the [N II]/Hα ratio decreasing as the extent increases. Since the ionizing radiation in BCGs likely to be generated from numerous sources (AGN, star formation, soft X-rays from the ICM, cosmic rays, shocks, collisional excitation etc.), this trend can be interpreted as an effect of the relative contributions of each. Radio observations of all BCGs in this sample have already been taken with a substantial number detected. Hogan et al. (2015) find a flat spectrum radio source at 10 GHz in 36 of the 73 objects in our sample, and a steep spectrum component at 1 GHz in 53/73 of our objects. This

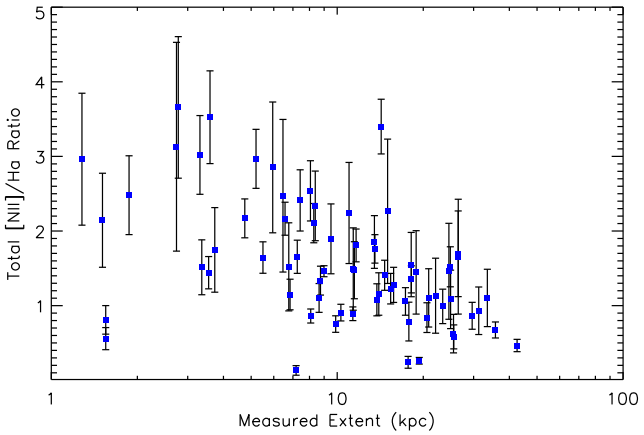

Figure 19. The overall [N II]/Hα ratio for every object in the VIMOS sample plotted against the extent of the line-emitting region. A loose trend can be seen in this plot which suggests that the overall [N II]/Hα ratio decreases as the extent of the emission line region increases. This suggests that the dominant source of the ionization is more energetic for compact objects than for extended ones. Likely, the compact objects feel more influence from a central AGN while the extended regions are ionized by other mechanisms.

suggests that AGN activity is currently active, or has recently been active within the cores of many of the BCGs in our sample. As such, in the very compact objects, the gas is likely to be concentrated near an AGN, so the ionization will thus be dominated by fast shocks and photoionization producing a high [N II]/Hα ratio. The more extended objects will have a higher relative contribution from other less energetic sources of ionization producing a lower overall ratio explaining the global trend we see in Fig. 19. In the next paper in this series, we will use resolved radio observations to compare the radio structure to the kinematics of the ionized gas to determine how the gas and AGN interact.

5.4 The source of the ionization

We have already discussed the ionization state of the gas in the previous section, however, it is important to note that while the [N II]/Hα ratio can provide a measure of how highly ionized any gas is, it cannot, on its own, be used to determine the source of the ionizing radiation. For this, other line ratios are also required, such as [O III]/Hβ for a BPT analysis (Baldwin et al. 1981). Unfortunately, for most of the objects in our sample, the observations did not cover the wavelength range required to observe these lines. However, as can be seen from Table 1, seven of the objects in our sample were at a redshift high enough to allow Hβ and [O III] to be present at the blue end of the HR_orange grism.

We produced BPT diagrams for the seven objects (Fig. 20) which had both Hβ and [O III] lines present in the spectrum. From Fig. 20, it is apparent that all seven of these objects appear to have ionization states which are not consistent with being the result of star formation activity based on the empirical separation from Baldwin et al. (1981) (dotted line). It is interesting to note that one of the objects for which the BPT analysis was possible was Abell 2566. Abell 2566 was discussed in Section 4.1.1 because the emission is completely offset from the BCG by ∼9 kpc. Kewley et al. (2001) calculate the maximum theoretical boundary for star formation which is shown as a dashed line in Fig. 20. We note that Abell 2566 falls below this line, within the region enclosed by the two dividing lines which Kewley et al. (2006) define as a region of composites between AGN and star formation (SF) ionization. Most of the points sampled in the other six of our seven objects fall above or on this line suggesting that star formation alone cannot explain the ionization. These objects show line ratios typically attributed to AGN. While this is not unexpected as BCGs do often host AGN (Hlavacek-Larrondo et al. 2013; Russell et al. 2013), there are also other processes which could produce the line ratios seen, shocks (Allen et al. 2008) or particle heating (Ferland et al. 2009; Fabian et al. 2011), for example. Additionally, we note that the $\log_{10}$([O III]/Hβ) values typically fall below ∼0.5 putting these objects in the region typically occupied by LINER-like objects which Singh et al. (2013) suggest do not require an AGN as the ionizing source. If AGN are responsible for ionizing the gas in all these systems, then this would suggest that the influence of the AGN is able to reach far beyond the core of the galaxy.

While the [O III] and Hβ lines were not covered by all of our observations, the [O I] and [S II] lines appear in many of the observations by virtue of being close in wavelength to the principal Hα line. While these lines are not as good an indicator of the mean level of ionization and temperature as [O III]/Hβ, their ratio with Hα are indicators of the relative importance of high-energy ionization in large partially ionized regions (Osterbrock 1989). These lines were detected in the extracted spectrum in the majority of our sample (see Appendix F for a list of line fluxes) allowing us to make some measure of the importance of high-energy ionization sources within the cores of clusters. In Fig. 21, we show histograms of the ratio of [N II], [S II] and [O I] with Hα and note that most ratios fall above the division between low- and high-energy ionization (Osterbrock 1989; Kewley et al. 2006).

In Fig. 22, we plot the [N II]$_{\lambda6583}$/Hα ratio against the [O I]$_{\lambda6300}$/Hα ratio. The [O I]$_{\lambda6300}$/Hα ratio shows a clear separation between sources ionized by low-energy sources (such as UV emission from star formation) and those ionized by other sources (such as AGN or shocks). Kewley et al. (2006) shows this divide occurs at approximately $\log_{10}$([O I]$_{\lambda6300}$/Hα) = −0.9 with all their sources above this value being from non-stellar processes. This is shown as a vertical line on Fig. 22. Similarly for the [N II]$_{\lambda6583}$/Hα ratio, Osterbrock (1989) shows a divide at approximately $\log_{10}$([N II]$_{\lambda6583}$/Hα) = −0.2. While this separation is less obvious since at higher values of $\log_{10}$([O III]$_{\lambda5007}$/Hβ), lower values of $\log_{10}$([N II]$_{\lambda6583}$/Hα) are seen, it is still true that all objects above this value in the Osterbrock (1989) sample are from AGN. Thus, without access to [O III] or Hβ, we use it as a first-order estimate of the separation and show it in Fig. 22 as a horizontal dashed line.

It is immediately apparent from Fig. 22 that the majority of the points fall in the upper right quadrant suggesting they are high-ionization regions dominated by excitation from non-star formation processes. It is not surprising then that a lower fraction of the core regions fall below these cut offs than the regions containing extended or total emission (9/73 compared to 13/73 and 14/73, respectively).

We show a comparison of the [S II]$_{\lambda6716+6731}$/Hα ratio against the [O I]$_{\lambda6300}$/Hα ratio in Fig. 23. Like the [O I]$_{\lambda6300}$/Hα ratio, [S II]$_{\lambda6716+6731}$/Hα shows a clear separation between sources ionized by high-energy photons (such as from narrow-line AGN) and those ionized by other sources (Osterbrock 1989). Like the [N II]$_{\lambda6583}$/Hα, the separation point shows some variation at high values of [O III]$_{\lambda5007}$/Hβ, but as the BPT diagrams in Fig. 20 suggest this is generally not the case in our sample, we adopt the value $\log_{10}$([S II]$_{\lambda6716+6731}$/Hα) = −0.4 as the separation between high-energy ionization regions and low-energy ionization regions. This is the maximum value that a H II region had in the sample of Osterbrock (1989), above this value all sources were ionized by

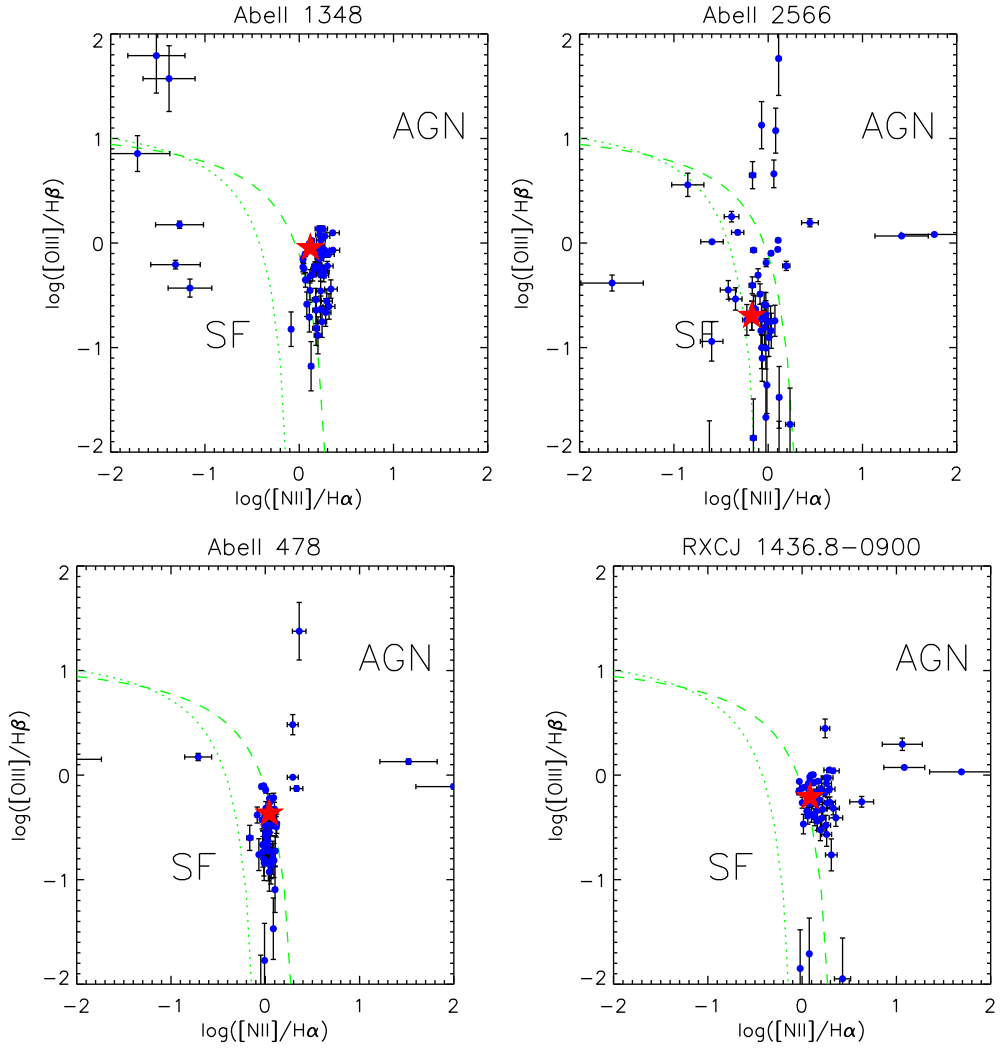

Figure 20. Here we show the BPT analysis of the objects from our sample which have redshifts that allow us access to the [O III] and Hβ lines in our VIMOS observations. The blue points show the locations of every pixel of detected emission on the diagram, the red stars then show the location of the central 2×2 arcsec^2 which should be the location of the AGN. The green dotted line marks the empirical boundary between star formation and AGN-dominated ionization while the green dashed line marks the theoretical upper limit of star formation dominated ionization. The region between these two lines likely contains objects which are a composite of star formation and AGN ionization. Note that, for Abell 2566, the emission was offset so the central region was determined from the Hα emission and not the continuum.

non-stellar processes. We plot this separation as a horizontal dashed line on Fig. 23 along with the same separation for the $[O\,I]_{\lambda6300}$/Hα ratio as used earlier. Once again, the objects show a clear trend towards higher values of both ratios suggesting the ionization is dominated by high-energy processes such as AGN or shocks. Like for $[N\,II]_{\lambda6583}$/Hα, we see a lower fraction of core regions (7/73) fall below these cut offs than the regions containing extended (15/73) or total (15/73) emission.

In Fig. 24, we compare the $[N\,II]_{\lambda6583}$/Hα and $[S\,II]_{\lambda6716+6731}$/H$\alpha$ ratios. Once again, the dashed lines represent the separation between high-energy ionization and low-energy ionization regions. The majority of the points fall above both cut offs again (with only 8/73 cores, 9/73 extended regions and 12/73 totals falling below the cut offs) suggesting that the gas is excited by more energetic processes. Interestingly, the points above both separating values show a much tighter correlation than is seen when either ratio is compared with $[O\,I]_{\lambda6300}$/Hα. The reason for this is not clear, however, we do note that $[O\,I]_{\lambda6300}$ is the weakest line used for this analysis and as such has larger measurement errors than the other lines. This may be responsible for introducing additional scatter in the other comparison plots, but we note that there is considerably more scatter below the cut-off values in Fig. 24, which is comparable to that seen in the other comparison plots.

Using the results from all three of these plots, we can categorize the 73 objects in our sample (separated into total emission, core emission and extended emission) based on all three line ratios. We classify star-forming objects as those whose ratios fall below the cut-off values for all three ratios, AGN-like objects (those excited by AGN or other high ratio producing mechanisms) have all three ratios above the cut-off values, ambiguous objects have at least one ratio above and at least one below the cut offs and unclassified objects have one line missing (due to absorption, falling outside the spectral coverage or just being too weak to detect) preventing analysis using all three ratios. According to this scheme, our sample contains five objects whose total emission is consistent with star formation, separating the cores and extended emission shows that

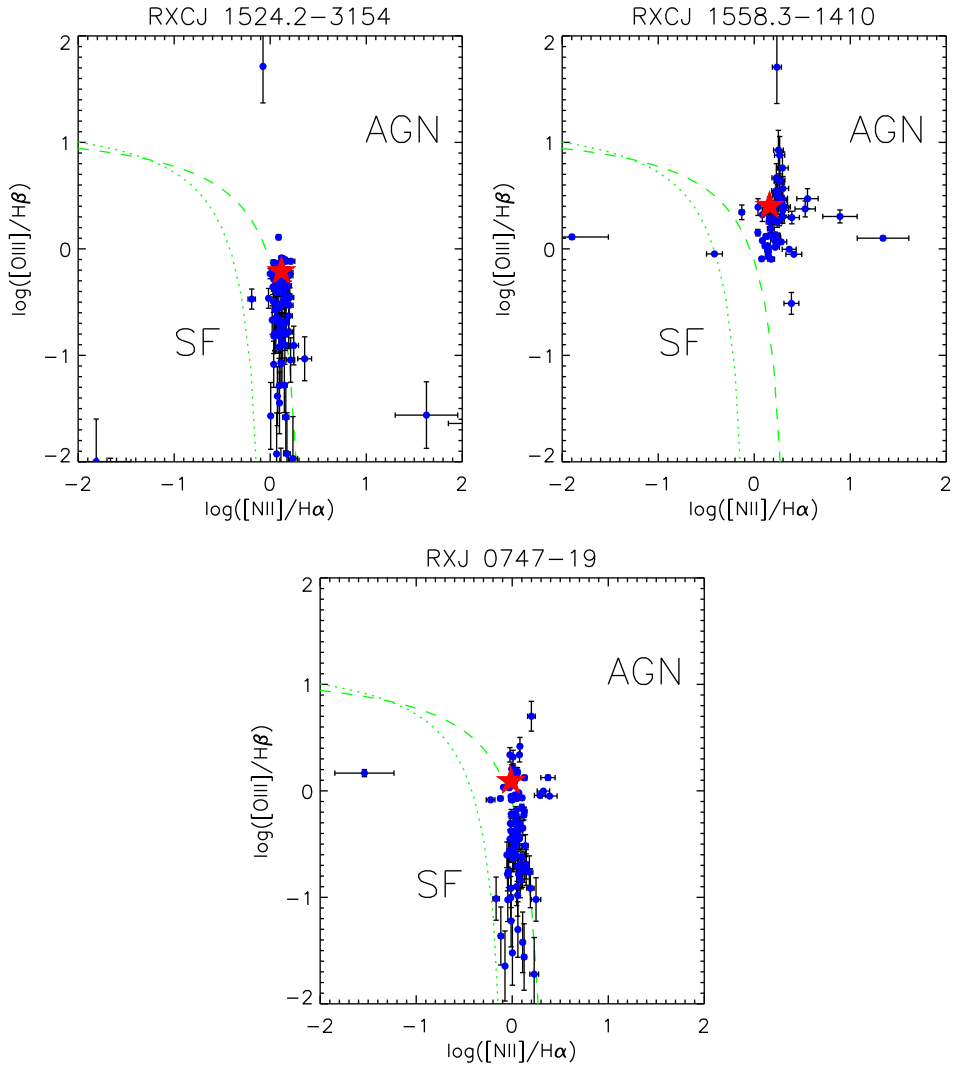

Figure 20 – *continued.*

only 3 cores are dominated by star formation while the number of extended regions rises to just six. By contrast, 46 objects have a total emission consistent with AGN like excitation, with 47 cores and 41 extended regions also showing AGN-like excitation. We find that 18 objects have ambiguous ratios in their total emission, with 10 cores and 16 extended regions also being ambiguous when analysed separately. Finally, we find the emission of 4 total regions, 13 cores and 10 extended regions cannot be classified due to having at least one line missing from their spectrum.

Some care must be taken when interpreting these ratios, in particular, the presence of any extreme outliers. Due to the range in redshift, some objects in the sample showed atmospheric absorption features in the region of their spectra containing these principle lines. For some objects, this was very apparent as a dip of the spectra to negative values. However, this was not always the case especially in systems with strong lines. Fortunately, the relatively narrow absorption feature and large redshift range mean that this problem only affects a handful of objects in the sample. We do not include objects affected by this absorption in our plots, thus allowing us to draw general conclusions from the overall statistics. Importantly, the majority of the points fall above the transition values between low- and high-energy ionization regions for all lines suggesting that the gas ionization is not dominated by star formation within the BCG. This is consistent with our BPT analysis presented earlier and with previous studies of line ratios in cluster cores (Johnstone & Fabian 1988; Crawford & Fabian 1992).

AGN are expected to be present in the cores of BCGs (Hlavacek-Larrondo et al. 2013; Russell et al. 2013) and are thus a potential source of the ionization seen, especially in the core regions. However, it is important to note that the extended regions of the ionized nebula in clusters can reach out over tens of kiloparsec from the core of the BCG. This would require the AGN to remain the dominant ionizing radiation source over many orders of magnitude in scale. Shocks could be present throughout the gas and can produce the line ratios seen. However, comparing to the shock models of Allen et al. (2008), our objects would require shocks over a larger range of velocities (100–1000 km s^{-1}) to fully explain all the line ratios seen. We would expect high-velocity shocks to be visible as regions of enhanced linewidth. While the central regions of our objects do show linewidths (FWHM) sufficiently broad to be consistent with such shocks, most objects have FWHM of the order of ∼100–200 km s^{-1} in their extended regions, suggesting that the fast shocks needed to produce the line ratios seen are not present here. The line ratios also do not agree well with the shock models of

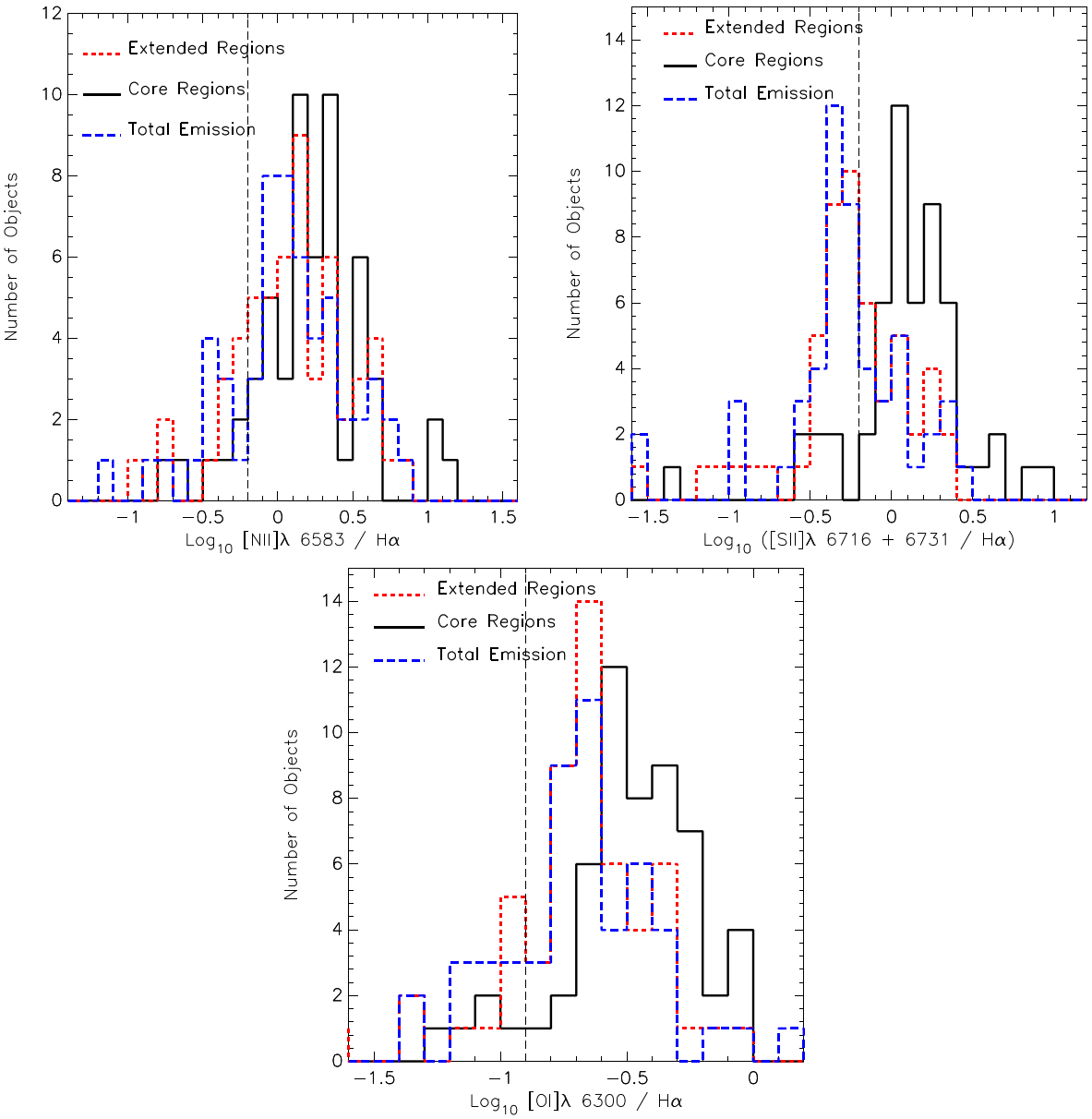

Figure 21. Histograms of the [N II] (left), [S II] (right) and [O I] (bottom) to Hα ratios for all object in the sample. The ratios from the total emission as well as from the extended and core regions are shown separately to allow for easy comparison. The vertical long dashed line shows the division between low- and high-energy ionization for each line ratio. Note that core regions typically fall at higher ratios suggesting they are ionized by more energetic sources such as AGN or shocks implying an AGN is at least partially responsible for the elevated ratios.

Allen et al. (2008). Of the seven objects with [O III] and Hβ detections, only one has an [O III]/Hβ ratio high enough to be consistent with a shock in excess of 300 km s^{-1}. From Fig. 21, we see that the majority of the $\log_{10}$([N II]/Hα ratios fall within 0.0–0.5 which are consistent with those expected for shocks ($\sim$0.0–0.4) however, the $\log_{10}$([O I]/Hα) ratios are mostly below -0.3 making them inconsistent with the values expected for shocks (~ -0.3 to 0.2). The $\log_{10}$([S II]/Hα) ratios for the majority of extended regions (-0.5 to 0.0) are consistent with those expected for shocks (~ -0.5 to 0.0) but the core regions are not (0.0–0.4). As such, there is no consistent evidence that shocks play a major role in the excitation of the gas.

Other sources of excitation within cluster cores (particle heating; for example, Ferland et al. 2009; Fabian et al. 2011) are therefore required to contribute significantly to the excitation of the gas. This can explain how the line ratios can remain relatively consistent throughout the gas, over a range of different scales, linewidths and average line ratios. This also explains how the ionized gas in Abell 2566 shows evidence of AGN-like ionization despite being offset from the BCG (and thus, far from the AGN) and having narrow linewidths. While AGN, shocks and star formation may not be the main source of the ionization, they are likely present in at least some of our objects leading to local variations of line ratios within a given object and can thus explain why some objects do show local variations while others do not. In particular, the trend towards higher average line ratios in more compact objects seen in Fig. 19 suggests that while other mechanisms are likely dominating the excitation of the gas globally, the AGN still plays a role.

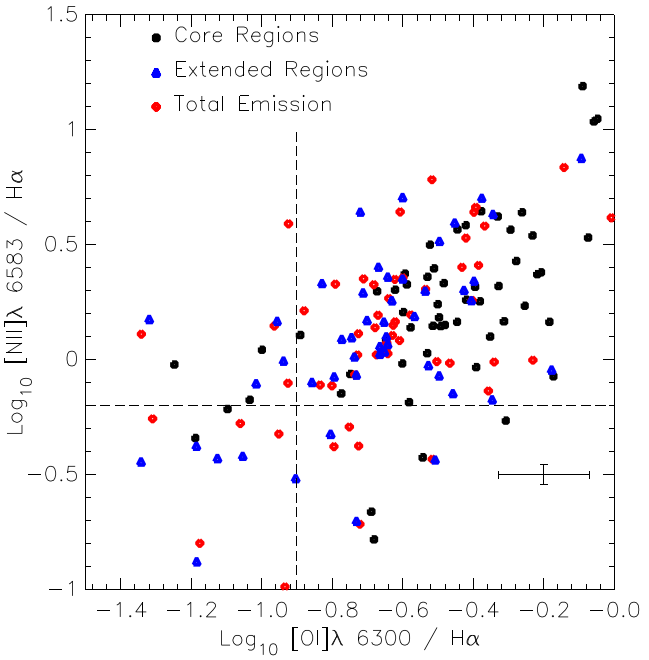

Figure 22. A comparison of the [N II]/H α and [O I]/H α ratios for all objects in the sample which had detections of all three lines. The points show the core regions (black squares), extended regions (blue triangles) and total emission (red diamonds) for each object. The dashed lines indicate the level above which empirical evidence suggests ionization is caused by non-stellar processes such as AGN or shocks. The majority of sources fall within the upper-right- hand quadrant, this is especially true for the core regions which show only nine objects falling below one of these lines and only two falling beneath both.

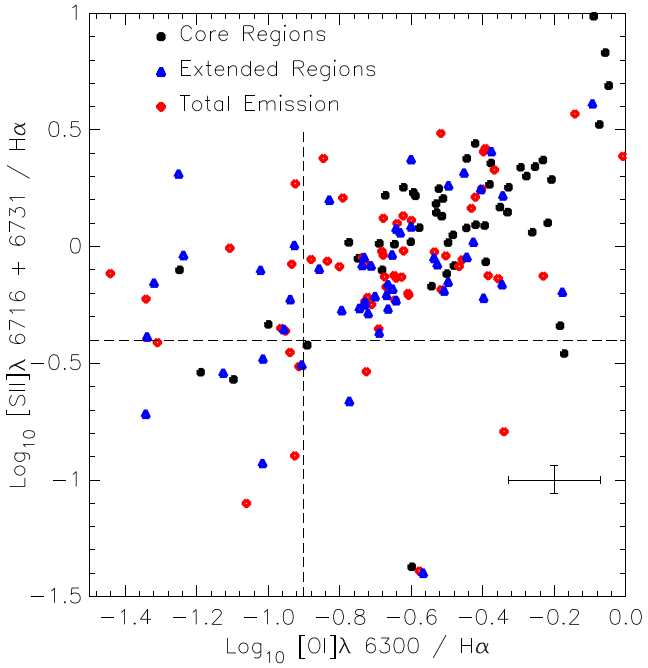

Figure 23. A comparison of the [S II]/H α and [O I]/H α ratios for all objects in the sample which had detections of all three lines. The points show the core regions (black squares), extended regions (blue triangles) and total emission (red diamonds) for each object. The dashed lines indicate the level above which empirical evidence suggests ionization is caused by non-star formation processes. The majority of sources fall within the upper-right-hand quadrant, this is especially true for the core regions which show only seven objects falling below this for one of these ratios and only two falling beneath both.

6 DISCUSSION

6.1 What fraction of line-emitting BCGs are highly disturbed

Our analysis showed that the extent of the line-emitting gas in cluster cores varies widely from system to system. A few objects are barely resolved by VIMOS, their extent dominated by the seeing of the observations with their line emission concentrated at the centre of the BCG. From the full sample of 73 objects, only Abell 194 appeared to be truly compact (extent $\leq$ seeing) in all directions. A further two were compact along a single axis but showed extent along the other. However, the majority of the objects had a true extent of the order of 5–20 kpc with a few extending out to 50 kpc (S780, Z348 etc.) to where the line emission far outshines the stellar continuum.

From the full sample, we identify five distinct morphological states. The compact objects described above account for the smallest fraction. While it is possible that these objects do have structure, it would require higher resolution observations taken in better seeing conditions to detect it. Offset objects, in which the peak and majority of the line emission is centred off, the BCG accounts for 4 of the 73 objects. Two of these objects were studied in detail in Hamer et al. (2012) and it was found that the offset line emission was co-spatial with the peak of X-ray emission from the ICM. Another ∼15 per cent (10/73) of the sample showed plumes of H α emission which had a bright peak centred on the BCG but also showed a clear extent in one preferential direction. For one object (Abell 3880), this plume appears to lead to another object within the VIMOS field of view. However, we note that this object shows spectral absorption lines at $z = 0$ clearly identifying it as a foreground star. One possible explanation for plumes is that they are caused by a cooling wake similar to that proposed by Fabian et al. (2001) as the origin of the long filaments in Abell 1795. While in Abell 1795, the resulting H α emission appears as long filaments that we do not see in our plumes, we note that the thickness of the filaments in Abell 1795 is significantly smaller to our mean seeing and all our plumed objects are of comparable or greater redshift than Abell 1795. As such, the seeing may be blending the filaments together in our observations producing the plumes that we see. A dedicated study of these objects combining high-resolution X-ray and H α observations and comparing to Abell 1795 would be needed to confirm this.

Disturbed objects have line emission that peaks close to the centre of the BCGs continuum peak but also shows extended non-uniform structures at lower surface brightness. There are 13 such objects (∼18 per cent) present in the sample which suggests that they are not common amongst the BCG population. It is possible that their prevalence in previous studies is a result of choosing to observe the most extreme systems. Indeed, the most common type of morphology seen in our sample are quiescent, simple elliptical systems which are concentrated towards the centre of the BCG. More than 60 per cent of the sample (45/73) show a quiescent morphology suggesting that major events (such as interactions) which can disturb the gas are relatively rare and that many systems remain undisturbed for long periods of time.

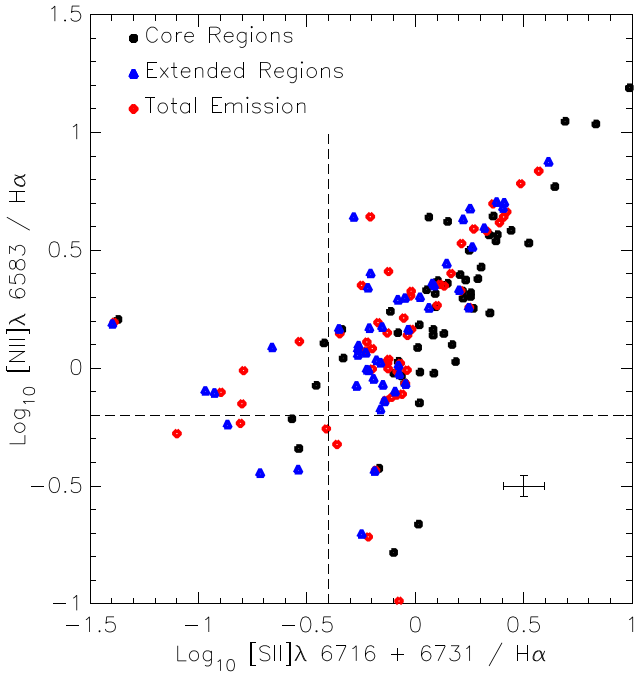

Figure 24. A comparison of the $[S\,II]_{\lambda6716+6731}/H\,\alpha$ and $[N\,II]_{\lambda6583}/H\,\alpha$ ratios for all objects in the sample which had detections of all four lines. The points show the core regions (black squares), extended regions (blue triangles) and total emission (red diamonds) for each object. The dashed lines indicate the level above which empirical evidence suggests ionization is caused by non-star formation processes. The majority of sources fall within the upper-right-hand quadrant, suggesting that non-stellar processes dominate the excitation.

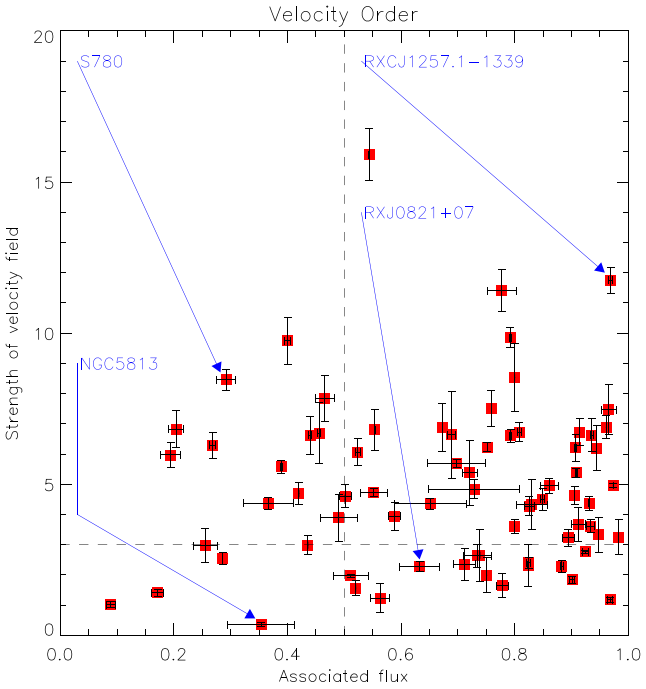

Figure 25. A comparison of the strength of the ordered structure in the velocity field (measured in standard deviations of the residuals) against the flux associated with the velocity field as a fraction of the total flux. The horizontal dashed line separates the strength of the velocity fields at $3\sigma_{\rm vel-resid}$, while the vertical dashed line separates the associated flux at 50 per cent. One object from each quadrant is labelled to allow comparison with the velocity maps. More than half our objects fall into the upper-right-hand quadrant suggesting that the majority of their H α emission is associated with a strong velocity field.

One caveat that must be considered, however, is that the observations of the sample are not able to resolve the filamentary structures seen in narrow-band imaging of objects such as NGC 5044 (Sun 2012) and NGC 1275 (Conselice et al. 2001). Such filaments are thought to be created when gas is uplifted through AGN feedback as the expanding radio lobe entrains the gas. The filaments in NGC 5044 appear as an extended, non-uniform low-surface brightness emission region in our IFU observations and make the system appear disturbed. It is possible that several of the other disturbed systems in our sample are similar to NGC 5044 with filamentary structures throughout their extended emission. We do identify the presence of filaments of H α emission in six objects, Abell 3378, Abell 3998, Abell 85, RXCJ 0120.9−1351, RXCJ 1304.2−3030 and S 805. While it is possible that these are related to the filaments seen in narrow-band observations, we note that the apparent thickness of these structures is substantially higher than that of those observed with narrow-band filters. While this may be an effect of the poorer seeing of our observations, these systems would have solitary long filaments, more like those of Abell 1795 (McDonald & Veilleux 2009) than NGC 1275 or NGC 5044.

The kinematics of the ionized gas is also an important indicator of how disturbed the system is. The mean velocity maps produced by the fitting routine allow us to directly examine the line-of-sight velocity structure of each object. The velocity structure of the ionized gas in two-thirds of the sample appears highly organized within the central regions with most objects showing a continuous velocity gradient across the brightest region of the H α emission which is typically coincident with the BCG.

To test the significance of this ordered velocity structure, we produced a simple model velocity field for each object following a single velocity gradient through the peak of the H α emission and adjusted the position angle (PA) and gradient to minimize the residuals with the H α velocity map. We define the disorder in the velocity map to be the standard deviation of these residuals ($\sigma_{\rm vel-resid}$). We calculate the strength of the velocity field as the peak–to–peak velocity divided by $\sigma_{\rm vel-resid}$ and the region of the line emission associated with the velocity gradient as having residuals less than $\sigma_{\rm vel-resid}/3$. We compare the strength of the velocity field with the fraction of the H α flux associated with it in Fig. 25. More than half our objects (40 out of 73) fall in the upper-right-hand region of this plot (velocity field strength greater than 3 and more than half the H α flux associated with the velocity gradient) suggesting that the majority of their H α emission is associated with a strong, ordered velocity field. We note that taking a velocity field strength of 2 as the dividing limit places roughly two-thirds of our objects in this category consistent with our visual inspection. This may not be an unrealistic assumption given that we use a very simple model for the velocity field and it is likely that a more sophisticated model would have lower residuals and thus the value of the peak-to-peak velocity divided by the standard deviation would be higher.

The more extended low-surface brightness emission present in some systems does not seem to share this ordered line-of-sight velocity structure, showing a much more random and disturbed distribution of velocities. We would expect to see increased linewidths in regions of the gas which is turbulent and disturbed. However, the outer regions in most systems appear to have low linewidths

which are relatively uniform suggesting that this is not the case. It is important to note that in systems with a large line-of-sight velocity shift, the coarse spatial sampling can result in artificially broadened lines but we determine this effect will be negligible given the linewidths and velocity gradients measured (see Fig. 13 and the related discussion).

A number of systems (9/73) showed multiple velocity components in their line emission. Typically, these additional components are very broad-line emission (8/73) in the very central regions of the BCG on scales comparable to the seeing and are most likely emission from the nuclear regions where gas is feeding on to the AGN. Indeed, this is expected as the presence of strong radio sources within the BCGs of many clusters which suggests that cold gas is actively being accreted in many systems. More interestingly however, two of our 73 objects showed multiple narrow line components similar to those found in Abell 1664 (Wilman et al. 2006, 2009). These objects were Abell 3574 and NGC 5044 and the two are very different. NGC 5044 shows a double component in its core regions (in addition to a broad line) while Abell 3574 has a double component ring of gas which surrounds its core. The full interpretation of these double component systems requires more data but suggests the ionized gas may be much more disturbed in a small fraction (∼3 per cent) of systems.

6.2 What role does the BCG play in the cooling of gas from the ICM?

In Hamer et al. (2012), we studied several objects in detail and determined that (for that sub-sample at least), the offset H α emission was coincident with the peak of the X-ray emission from the ICM. Our analysis of the X-ray – optical line offsets in Section 4.1.1 would appear to confirm this result as at most 3 of the 24 objects studied showed a potential significant offset of the H α emission from the peak of the X-rays. The analysis of the structure of the full sample presented in this paper does identify several more objects which show an offset between the H α and continuum peaks. Hamer et al. (2012) were able to associate the offset peak with evidence of gas sloshing (Johnson et al. 2010, 2012; ZuHone, Markevitch & Johnson 2010; Blanton et al. 2011; ZuHone, Markevitch & Lee 2011) in the ICM as well as continued cooling at the position offset from the BCG. However, in these additional systems, the multi-wavelength data necessary to make this determination (deep X-ray imaging and/or resolved CO detections) were not available, so we cannot say if this is true for all offset systems. Despite this, it is apparent that offset line emission, while still rare (4/73 systems), is more common than initially thought and may thus play a more significant role in the evolution of the cluster core.

In a small number of objects, the stellar continuum was sufficiently bright to allow us to extract the stellar kinematics from the BCG. Comparing the maps of the stellar kinematics to the gas kinematics, it is apparent that the line-of-sight velocity structure of the stellar component is negligible, in stark contrast to the high-velocity, ordered structures seen in the gas component. This suggests that the kinematics of the line-emitting gas are decoupled from those of the stellar population of the BCG implying that cooling gas is not necessarily related to the BCG even when cooling is occurring at the BCGs location.

This raises the question, if the gas is relaxed and stable why is it not forming stars and producing a stellar velocity field that matches that seen in the gas? Hydra-A has one of the most extreme H α velocity fields in our sample, the gas is contained in a rotating disc that is known to be forming stars at a rate of 2–3 M$\odot$ yr^{-1} (Donahue et al. 2011; Hoffer et al. 2012). If the disc is responsible for feeding the AGN (Hamer et al. 2014), then it must have been stable for the lifetime of the outburst (∼10^8 yr for an accretion rate of 0.1–0.25 M$\odot$ yr^{-1} and a total accreted mass of 10^7 M$\odot$; Wise et al. 2007). Assuming the star formation rate is constant during this time, then the total mass of stars the disc will form is 3×10^8 M$\odot$, which is a negligible fraction of the typical stellar mass of a BCG (10^{11}–10^{12} M$\odot$). Thus, the stellar velocity field we observe is dominated by the bulk of the stellar component formed in previous generations of star formation, which need not share the current velocity field of the gas.

6.3 What role does the cold gas play in fuelling feedback?

Mechanical feedback from AGN outbursts within BCGs is commonly believed to be the main contributing factor preventing the catastrophic cooling of gas in cluster cores. A requirement for this process to work effectively is a mechanism of self-regulation to maintain the balance between cooling gas and feedback. Thus a link must be established between the gas cooling (on kpc scales) and its supply to the supermassive black hole which results in the activation of the AGN once cooling reaches a critical threshold. In Hamer et al. (2014), we show that one system (Hydra-A) in our sample has kinematics in the ionized gas that clearly trace the presence of an extended (∼5 kpc) disc of cold, molecular and atomic gas in the core of the system. Such a disc can potentially channel gas to the centre of the system relatively quickly allowing it to fuel the AGN. The confirmation of the disc in Hydra-A was made possible thanks to the system being relatively close by, having a large velocity shift and being viewed at close to edge-on. Our analysis of the velocity gradients suggest that this sample is consistent with a sample of rotating discs similar to the one seen in Hydra-A and Fig. 25 suggests that >50 per cent of systems have the bulk of their H α emission associated with this velocity gradient. However, confirming the presence of a disc within each individual system requires a more sophisticated, case-by-case analysis (which will be presented in paper II; Hamer et al. in preparation).

From the velocity dispersion maps, it is apparent that the linewidths are typically broadest towards the peak of the H α emission which is consistent with this position having the longest line of sight through the gas and thus sampling the widest distribution of velocity components. We note that the FWHM, in the central regions, is typically of the order of the velocity shift across the whole system, suggesting it originates from the extended gas in the ionized nebula. However, 8 of the 73 systems show some evidence of very broad (FWHM of the order of 2355 km s^{-1} or more) components localized (on scales of the seeing) to their central regions. This can be interpreted as emission from an AGN suggesting that the AGN in these systems are actively accreting. However, we note that the broad component is typically very weak and the scales of the seeing are much greater than those expected for an AGN, making this difficult to confirm without deeper, higher resolution observations.

6.4 The source of the ionization

The maps of the [N II]$_{\lambda6583}$/H α ratio produced in Section 4 show a wide variation in value between objects. More interestingly, perhaps the ratio is seen to vary within a given object suggesting that the source of the ionizing radiation may not be uniformly distributed. Likewise, it shows no trend radiating from a single point suggesting that the dominant source of the ionization is not a single localized source but is more homogeneously spread throughout the cluster

core. Given the extended nature of these sources, and the variation seen within different regions of individual objects, it seems unlikely that an AGN positioned at the centre of the BCG could be responsible for the ionization throughout the nebula. However, the trend that more compact objects typically show higher line ratios than extended objects does suggest that AGN still play a role in the excitation of the gas even if it is not dominant. We therefore conclude that other, more diffuse, sources must also be significantly contributing to the excitation of the gas.

Star formation is (along with AGN) the most commonly invoked excitation mechanism and has the potential to be distributed throughout the BCG. For the few objects (just seven, less than 10 per cent of our sample) in which we had access to the Hβ and [O III] lines and we perform a BPT analysis (Baldwin et al. 1981) to look for evidence of excitation by star formation. This analysis suggests that the gas in all of these objects is predominantly ionized by non-stellar processes and is, as such, inconsistent with excitation by star formation. Analysis with other spectral indicators (the [NII/Hα], [S II]/Hα and [O I]/Hα emission line ratios) also indicates that non-stellar processes dominate the ionization of the gas in most systems. These line ratio diagnostics are all consistent and rule out star formation as the dominant excitation mechanism in the vast majority of objects in our sample.

Shocks also seem to be an appropriate candidate for a distributed excitation mechanism, however, we note that the velocity dispersion maps do not show evidence of shocks of sufficient velocity in the extended regions (seen as enhanced linewidths) to produce the line ratios seen. Comparison of the measured line ratios with those predicted by shock models also shows no consistent evidence that shocks are a major contributor to the gas excitation for the objects in our sample. The most likely candidate then is particle heating caused by a reconnection of the gas phases (Ferland et al. 2009; Fabian et al. 2011). This can also explain the presence of ionized emission in offset objects which have bright line emission coincident with their X-ray peaks (Hamer et al. 2012) but are displaced from the bulk of the BCGs stellar component. We note, however, that AGN still play a role in the excitation of the gas and indeed other sources of excitation, such as cosmic rays, shocks and star formation, are likely also contributing to the overall ionization state of the gas. All of these processes, and their interaction, need to be considered to fully understand the excitation of the gas.

7 CONCLUSIONS

We have analysed the morphology, kinematics and excitation of the optical line-emitting nebula in a sample of 73 BCGs with the VIMOS IFU. Our goal has been to develop a more complete understanding of the nature of these ionized nebula, what role they play in the physical processes affecting the cluster core and what they can tell us about the interaction of the BCG with the ICM. Throughout this paper, we present a number of results that can be used to address these issues which we will now summarize.

(1) We classify our objects into five categories based on the morphology of their optical line-emitting nebula. While we do find that some objects appear disturbed (13/73), the majority of our sample have elliptical, centrally concentrated morphologies (45/73) suggesting that the gas is in a relatively quiescent, undisturbed state (Section 4.1).

(2) We detect a number of systems in which the peak of the line emission is offset from the BCG. Some of these objects where already known and they are typically found in systems in which the ICM is 'sloshing' (Hamer et al. 2012) suggesting that the gas in the ICM has been disturbed. The number of these objects in our sample is small (4/73) suggesting that such major disturbances are rare (Section 4.1.1).

(3) The extent of the nebulae varies quite considerably between objects but can extend out over several tens of kpc in some objects. While previous narrow-band studies suggest we might expect to see complex filamentary structures in these extended regions, we are unable to resolve the filamentary structures in most objects. However, in some systems, we do detect isolated filaments which may be related and only detectable because they are isolated and thus not blurred with other filaments as a result of the seeing (Section 4.1).

(4) The majority of our objects show gas with a high line-of-sight velocity in the form of a velocity shift that runs across the ionized nebula. This velocity structure is visible in the velocity maps (Section 4.2) but it is also visible in the channel maps (Section 3) where the position of the gas can be seen to vary smoothly with channel.

(5) The velocity structure of the gas in most systems appears quite ordered and typically varies little away from the main velocity shift that runs across the nebula (Section 4.2). This is especially apparent when we consider the strength of this velocity shift against the fraction of the Hα flux that it represents (Fig. 25), and we find that, in 40/73 of our objects, more than half the Hα flux is associated with a strong velocity shift.

(6) When measuring the gradient of the velocity shifts observed, we find that the gradient shows a clear relationship with the separation of the maximum and minimum velocities but none with the magnitude of the velocity difference. The relationship we measure is inconsistent with random motions suggesting that the measured velocity along the velocity shift is a function of distance from the BCG (Section 4.2).

(7) The velocity dispersion maps of the gas show that the linewidth typically peaks towards the centre of the nebula but is otherwise low ($\sim$100–200 km s^{-1}) in the more extended regions (Section 4.2.1).

(8) We show that the total Hα luminosity and extent of the line-emitting nebula are well-correlated. This coupled with the fact the velocity of the gas appears related to the distance from the core of the BCG suggests that the magnitude of the velocity shift should be related to the Hα luminosity. By assuming that differences in the velocity shift at a given luminosity are caused by inclination, we are able to reproduce an inclination distribution consistent with what is expected for a random sample such as this (Section 4.3).

(9) By measuring the stellar kinematics from the NaD absorption feature, we show that the stars do not have a strong velocity shift, or any obvious velocity structure, like those seen in the gas. This suggests that the velocity field of the stars is dominated by random motions and is thus decoupled from the gas component (Section 4.4).

(10) The maps of measured line ratio ([N II]/Hα) show a considerable amount of variation within each nebula. However, importantly, they show no obvious trend or ordered structure suggesting that the source of the excitation is not localized to a specific region of the nebula (Section 5.3).

(11) By comparing the global [N II]/Hα ratio for each object to the extent of the line-emitting nebula, we find a loose trend that objects with a smaller extent have higher line ratios. This implies that more compact objects are preferentially excited by more energetic sources

suggesting that AGN may be playing some role in the excitation of the gas, at least in the central regions of the BCG (Section 5.3).

(12) We perform line ratio diagnostics on the gas to determine the source of the excitation, and find that for most objects in our sample, it is inconsistent with star formation. We are also unable to find any consistent evidence that shocks are playing a significant role in the excitation (Section 5.4).

These results allow us to draw several conclusions about the nature of the ionized gas within cluster cores. The fact that the majority of objects have an Hα morphology which suggests the gas is relatively quiescent (Point 1) suggests that the gas is typically not highly disturbed within most systems. Similarly while many objects do show gas at high velocities relative to the BCG, the structures of the high-velocity components appear well-ordered varying smoothly from blueshifted to redshifted across the nebula (Points 4 and 5). If the gas were disturbed, then we might expect to see evidence of shocks, caused by moving gas colliding with gas moving at different velocities, in the velocity dispersion maps. However, the velocity dispersion maps do not show evidence of enhanced linewidths away from the central regions (Point 7) suggesting that random motions are not significant within the extended nebula. We do see a number of systems with disturbed morphologies but these objects account for less than 20 per cent (13/73) of our sample (Point 1). These objects also typically show a more disordered velocity structure in the extended, low-surface brightness gas (e.g. Abell 3581, NGC 5044, RXJ 0338+09). We also identify several objects with offset emission similar to those studied in Hamer et al. (2012) (Point 2). While the nature of these objects clearly suggests they are disturbed, they account for a very small fraction of the overall population (just 4/73 of our objects). While a few of these disturbed systems did show evidence of a possible interaction with another cluster member (e.g. RXJ 0338+09), it was not a common factor in all disturbed systems. However, we cannot rule out the possibility that the gas was disturbed by a previous fly-by interaction with a galaxy that has since left the VIMOS field of view. Despite these systems, the majority of the BCGs in our sample have line-emitting nebula which are quiescent and ordered in both their morphology and kinematics suggesting that the gas is relaxed rather than disturbed within the bulk of the population.

The identification of several more objects with offset emission similar to those studied in Hamer et al. (2012) (Point 2) suggests that such offsets may be more common than previously thought. It is possible that the multiple velocity components seen in the cores of objects like Abell 1664 and NGC 5044 may be a related phenomena but a more detailed analysis of these objects is needed to confirm such a link. If these additional offset systems are similar to those presented in Hamer et al. (2012), then it suggests that sloshing may be present (albeit at different levels) in all systems and strengthens the conclusion that the BCG is not required for cooling gas to condense from the ICM despite the strong spatial correlation with the cluster core (Peres et al. 1998; Sanderson, O'Sullivan & Ponman 2009; Hudson et al. 2010). The fact that the gas does not share the kinematics of the stars (Point 9) also suggests that the stellar component of the BCG and the gas that make up the nebula are not linked and that the gas need not have cooled at its current location within the BCG. The large extent of some of the objects in our sample and the filaments seen may also support this (Point 3). While these structures may be the result of gas which has been removed from the BCG (either entrained by radio jets or blown out by winds), the fact that we see gas cooling away from the BCG in the offset systems suggests a different possibility. These filaments and extended regions could be the result of gas which has cooled from the ICM away from the BCG and is now falling towards it. Our current data do not allow us to test this hypothesis but with new instrumentation (Multi Unit Spectroscopic Explorer, Atacama Large Millimeter/submillimeter Array etc.), it should be possible.

The shift from positive to negative velocities across the brightest regions of the Hα seen in the majority of the systems in our sample (Point 5) is similar to the velocity structure found in Hydra-A (Hamer et al. 2014). We also note that the velocity gradients show evidence of being dependant only on the distance over which they are measured (Point 6). Such a velocity structure could be the result of a disc like rotation similar to that seen in Hydra-A and our estimations of the inclinations from the magnitude of the velocity shift at a given luminosity (Point 8) are consistent with the expected inclinations of a random sample of discs. This suggests that kpc scale discs may be common in cluster cores, however, we note that other phenomena can also produce velocity structures similar to those seen (bi-polar outflows for example), so a more detailed study is needed to confirm the presence of discs. If discs are common, this would provide a potential link between the gas cooling on kpc scales and the fuelling of the central black hole. The fact that the stellar and gas kinematics are decoupled (Point 9) seems to support this interpretation. If the gas is stable as it appears to be, then it should form stars which over the lifetime of the cluster would produce a stellar velocity field matching that of the gas. Thus gas discs such as the one seen in Hydra-A must be a transient phenomena and the gas must be disturbed or consumed before it can form a sufficient number of stars to affect the overall stellar velocity field. The main questions remaining then are whether the velocity structure seen in the gas within most BCGs relates to a disc and if it does, is the disc jet alignment seen in Hydra-A (Hamer et al. 2014) unique to that system or common to all BCGs with gas discs. We will address these questions in the next paper in this series by presenting a detailed analysis of the kinematics of each individual object and comparing to tracers of the AGN outbursts at radio and X-ray wavelengths.

From our study of the gas excitation, we conclude that a distributed process is the main component of the gas ionization as the line ratio maps show significant variation within a given object but no obvious trend from a given point to suggest a localized source (Point 10). Despite this, the global line ratios for each object are higher in more compact objects (Point 11) which suggests that an energetic source at the centre of the emission (most likely an AGN) is contributing to the excitation of the gas but is not the dominant component in the most extended regions. Through the use of line ratio diagnostics, we can rule out star formation as the dominant distributed excitation source (Point 12). The line ratio diagnostics also show no consistent evidence for shocks (Point 12) and the narrow linewidths seen in the extended emission suggest that the fast shocks needed to excite the gas to the levels seen are not present (Point 7). As such, we must appeal to particle heating (Ferland et al. 2009; Fabian et al. 2011) to explain the excitation in the extended nebula, though AGN (and likely other processes) still play a role.

This work represents a significant step forward in the study of the interplay between the brightest cluster galaxy, the cold gas in the cluster core and the cooling of the hot gas in the ICM. We have shown that despite the high velocity of the ionized gas, it typically forms simple and ordered spatial and kinematics structures. Such simple structures clearly favour a situation in which the gas has cooled from the surrounding medium and has remained undisturbed by interactions with other cluster members for some time.

ACKNOWLEDGEMENTS

SLH acknowledges support from the European Research Council for Advanced Grant Program num 339659–MUSICOS. FC acknowledges the support from the European Research Council for Advanced Grant Program num 267399–Momentum. AMS gratefully acknowledges an Science and Technology Facilities Council Advanced Fellowship through grant number ST/H005234/1 and the Leverhume foundation. ACE acknowledges support from Science and Technology Facilities Counci grant ST/I001573/1. HRR and ACF acknowledge European Research Council Advanced Grant Feedback. BRM acknowledges funding from the Natural Sciences and Engineering Research Council of Canada. JHL is supported by Natural Sciences and Engineering Research Council through the discovery grant and Canada Research Chair programs, as well as the Fonds de recherche du Québec – Nature et technologies.

Based on observations made with ESO Telescopes at the La Silla or Paranal Observatories under programme ID 080.A-0224 and 082.B-0671.

REFERENCES

Abell G. O., 1958, ApJS, 3, 211
Allen M. G., Groves B. A., Dopita M. A., Sutherland R. S., Kewley L. J., 2008, ApJS, 178, 20
Bahcall N. A., 1999, in Dekel A., Ostriker J. P., eds, Formation of Structure in the Universe. Cambridge Univ. Press, Cambridge, p. 135
Baldwin J. A., Phillips M. M., Terlevich R., 1981, PASP, 93, 5
Bica E., Pastoriza M. G., da Silva L. A. L., Dottori H., Maia M., 1991, AJ, 102, 1702
Blanton E. L., Randall S. W., Clarke T. E., Sarazin C. L., McNamara B. R., Douglass E. M., McDonald M., 2011, ApJ, 737, 99
Böhringer H., Werner N., 2009, preprint (arXiv: 0907.4277)
Böhringer H. et al., 2004, A&A, 425, 367
Bower R. G., Benson A. J., Malbon R., Helly J. C., Frenk C. S., Baugh C. M., Cole S., Lacey C. G., 2006, MNRAS, 370, 645
Braine J., Dupraz C., 1994, A&A, 283, 407
Burns J. O., Rhee G., Owen F. N., Pinkney J., 1994, ApJ, 423, 94
Cappellari M., Emsellem E., 2004, PASP, 116, 138
Cavagnolo K. W., Donahue M., Voit G. M., Sun M., 2008, ApJ, 683, L107
Cavagnolo K. W., Donahue M., Voit G. M., Sun M., 2009, ApJS, 182, 12
Churazov E., Sunyaev R., Forman W., Böhringer H., 2002, MNRAS, 332, 729
Conselice C. J., Gallagher J. S., III, Wyse R. F. G., 2001, AJ, 122, 2281
Courteau S., 1997, AJ, 114, 2402
Crawford C. S., Fabian A. C., 1992, MNRAS, 259, 265
Crawford C. S., Allen S. W., Ebeling H., Edge A. C., Fabian A. C., 1999, MNRAS, 306, 857
Crawford C. S., Gandhi P., Fabian A. C., Wilman R. J., Johnstone R. M., Barger A. J., Cowie L. L., 2002, MNRAS, 333, 809
Croton D. J. et al., 2006, MNRAS, 365, 11
David L. P. et al., 2011, ApJ, 728, 162
David L. P. et al., 2014, ApJ, 792, 94
Denicoló G., Terlevich R., Terlevich E., 2002, MNRAS, 330, 69
Donahue M., de Messières G. E., O'Connell R. W., Voit G. M., Hoffer A., McNamara B. R., Nulsen P. E. J., 2011, ApJ, 732, 40
Dopita M. A., Kewley L. J., Heisler C. A., Sutherland R. S., 2000, ApJ, 542, 224
Ebeling H., Voges W., Bohringer H., Edge A. C., Huchra J. P., Briel U. G., 1996, MNRAS, 281, 799
Ebeling H., Edge A. C., Bohringer H., Allen S. W., Crawford C. S., Fabian A. C., Voges W., Huchra J. P., 1998, MNRAS, 301, 881
Ebeling H., Edge A. C., Allen S. W., Crawford C. S., Fabian A. C., Huchra J. P., 2000, MNRAS, 318, 333
Edge A. C., 2001, MNRAS, 328, 762
Edwards L. O. V., Robert C., Mollá M., McGee S. L., 2009, MNRAS, 396, 1953
Fabian A. C., 1994, ARA&A, 32, 277
Fabian A. C., Hu E. M., Cowie L. L., Grindlay J., 1981, ApJ, 248, 47
Fabian A. C., Sanders J. S., Ettori S., Taylor G. B., Allen S. W., Crawford C. S., Iwasawa K., Johnstone R. M., 2001, MNRAS, 321, L33
Fabian A. C., Johnstone R. M., Sanders J. S., Conselice C. J., Crawford C. S., Gallagher J. S., III, Zweibel E., 2008, Nature, 454, 968
Fabian A. C., Sanders J. S., Williams R. J. R., Lazarian A., Ferland G. J., Johnstone R. M., 2011, MNRAS, 417, 172
Ferland G. J., Fabian A. C., Hatch N. A., Johnstone R. M., Porter R. L., van Hoof P. A. M., Williams R. J. R., 2009, MNRAS, 392, 1475
Hamer S. L., Edge A. C., Swinbank A. M., Wilman R. J., Russell H. R., Fabian A. C., Sanders J. S., Salomé P., 2012, MNRAS, p. 2520
Hamer S. L. et al., 2014, MNRAS, 437, 862
Hatch N. A., Crawford C. S., Fabian A. C., Johnstone R. M., 2005, MNRAS, 358, 765
Hatch N. A., Crawford C. S., Johnstone R. M., Fabian A. C., 2006, MNRAS, 367, 433
Heckman T. M., 1980, A&A, 87, 142
Heckman T. M., Baum S. A., van Breugel W. J. M., McCarthy P., 1989, ApJ, 338, 48
Heckman T. M., Lehnert M. D., Strickland D. K., Armus L., 2000, ApJS, 129, 493
Hlavacek-Larrondo J., Fabian A. C., Edge A. C., Ebeling H., Allen S. W., Sanders J. S., Taylor G. B., 2013, MNRAS, 431, 1638
Hoffer A. S., Donahue M., Hicks A., Barthelemy R. S., 2012, ApJS, 199, 23
Hogan M. T. et al., 2015, MNRAS, 453, 1201
Hudson D. S., Mittal R., Reiprich T. H., Nulsen P. E. J., Andernach H., Sarazin C. L., 2010, A&A, 513, A37
Jacoby G. H., Hunter D. A., Christian C. A., 1984, ApJS, 56, 257
Jiménez-Vicente J., Castillo-Morales A., Mediavilla E., Battaner E., 2007, MNRAS, 382, L16
Johnson R. E., Markevitch M., Wegner G. A., Jones C., Forman W. R., 2010, ApJ, 710, 1776
Johnson R. E., Zuhone J., Jones C., Forman W. R., Markevitch M., 2012, ApJ, 751, 95
Johnstone R. M., Fabian A. C., 1988, MNRAS, 233, 581
Johnstone R. M., Fabian A. C., Nulsen P. E. J., 1987, MNRAS, 224, 75
Katz N., White S. D. M., 1993, ApJ, 412, 455
Kewley L. J., Dopita M. A., 2002, ApJS, 142, 35
Kewley L. J., Dopita M. A., Sutherland R. S., Heisler C. A., Trevena J., 2001, ApJ, 556, 121
Kewley L. J., Groves B., Kauffmann G., Heckman T., 2006, MNRAS, 372, 961
Loewenstein M., 2004, in McWilliam A., Rauch M., eds, Origin and Evolution of the Elements. Cambridge Univ. Press, Cambridge, p. 422
McDonald M., Veilleux S., 2009, ApJ, 703, L172
McDonald M., Veilleux S., Mushotzky R., 2011, ApJ, 731, 33
McNamara B. R., Jaffe W., 1994, A&A, 281, 673
McNamara B. R., Nulsen P. E. J., 2007, ARA&A, 45, 117
McNamara B. R., O'Connell R. W., 1989, AJ, 98, 2018
McNamara B. R., Nulsen P. E. J., Wise M. W., Rafferty D. A., Carilli C., Sarazin C. L., Blanton E. L., 2005, Nature, 433, 45
Markevitch M., Vikhlinin A., 2007, Phys. Rep., 443, 1
Moré J., Wright S., 1993, Optimization Software Guide. Frontiers in Applied Mathematics, Society for Industrial and Applied Mathematics, Philadelphia
O'Dea C. P., Baum S. A., Maloney P. R., Tacconi L. J., Sparks W. B., 1994, ApJ, 422, 467
O'Dea K. P. et al., 2010, ApJ, 719, 1619
Osterbrock D. E., 1989, Astrophysics of Gaseous Nebulae and Active Galactic Nuclei, Univ. Sci. Books, CA
Owen F. N., Ledlow M. J., 1997, ApJS, 108, 41
Peres C. B., Fabian A. C., Edge A. C., Allen S. W., Johnstone R. M., White D. A., 1998, MNRAS, 298, 416
Peterson J. R., Fabian A. C., 2006, Phys. Rep., 427, 1

Peterson J. R. et al., 2001, A&A, 365, L104
Peterson J. R., Kahn S. M., Paerels F. B. S., Kaastra J. S., Tamura T., Bleeker J. A. M., Ferrigno C., Jernigan J. G., 2003, ApJ, 590, 207
Pettini M., Pagel B. E. J., 2004, MNRAS, 348, L59
Russell H. R., McNamara B. R., Edge A. C., Hogan M. T., Main R. A., Vantyghem A. N., 2013, MNRAS, 432, 530
Salomé P., Combes F., 2003, A&A, 412, 657
Salomé P., Combes F., Revaz Y., Downes D., Edge A. C., Fabian A. C., 2011, A&A, 531, A85
Sanders J. S., Fabian A. C., Taylor G. B., 2009, MNRAS, 396, 1449
Sanderson A. J. R., Edge A. C., Smith G. P., 2009, MNRAS, 398, 1698
Sanderson A. J. R., O'Sullivan E., Ponman T. J., 2009, MNRAS, 395, 764
Sarazin C. L., O'Connell R. W., McNamara B. R., 1992, ApJ, 397, L31
Simkin S. M., 1979, ApJ, 234, 56
Singh R. et al., 2013, A&A, 558, A43
Sun M., 2012, New J. Phys., 14, 045004
Tamura T. et al., 2001, A&A, 365, L87
Tempel E., Stoica R. S., Saar E., 2013, MNRAS, 428, 1827
Veilleux S., Cecil G., Bland-Hawthorn J., 2005, ARA&A, 43, 769
Voigt L. M., Fabian A. C., 2004, MNRAS, 347, 1130
Werner N. et al., 2014, MNRAS, 439, 2291
Wilman R. J., Edge A. C., Swinbank A. M., 2006, MNRAS, 371, 93
Wilman R. J., Edge A. C., Swinbank A. M., 2009, MNRAS, 395, 1355
Wilman R. J., Edge A. C., McGregor P. J., McNamara B. R., 2011, MNRAS, 416, 2060
Wise M. W., McNamara B. R., Nulsen P. E. J., Houck J. C., David L. P., 2007, ApJ, 659, 1153
ZuHone J. A., Markevitch M., Johnson R. E., 2010, ApJ, 717, 908
ZuHone J. A., Markevitch M., Lee D., 2011, ApJ, 743, 16

SUPPORTING INFORMATION

Additional Supporting Information may be found in the online version of this article:

Appendix A–F.
(http://mnras.oxfordjournals.org/ lookup/suppl/doi:10.1093/mnras/stw1054/-/DC1).

Please note: Oxford University Press is not responsible for the content or functionality of any supporting materials supplied by the authors. Any queries (other than missing material) should be directed to the corresponding author for the article.

This paper has been typeset from a TEX/LATEX file prepared by the author.